College of Science and Health Theses and Dissertations

College of Science and Health

Summer 8-19-2018

"EFFECT OF ZINC AND STRONTIUM DOPANTS ON THE STRUCTURE AND STABILITY OF HYDROXYAPATITE AT HIGH TEMPERATURES"

Dylan Correll Smith
DePaul University, dsmith@colgate.edu

Follow this and additional works at: https://via.library.depaul.edu/csh_etd

Part of the Physics Commons

Recommended Citation

EFFECT OF ZINC AND STRONTIUM DOPANTS ON THE STRUCTURE AND STABILITY OF HYDROXYAPATITE AT HIGH TEMPERATURES

———————————

A Thesis

Presented in

Partial Fulfillment of the

Requirements for the Degree of

MASTER OF SCIENCE

June, 2 0 1 8

BY

Dylan C. Smith

PHYSICS DEPARTMENT

College of Science and Health

DePaul University

Chicago, Illinois

TABLE OF CONTENTS

LIST OF FIGURES 4

LIST OF TABLES 8

ABSTRACT 9

CHAPTER 1   Introduction 11
   1.1   Background 11
   1.2   Crystallographic Structure 12
   1.3   Literature Review 15
   1.4   Motivation for this Study 17

CHAPTER 2   Experimental Procedure 19
   2.1   Sample Preparation 19
   2.2   X-ray Diffraction Measurements 19
   2.3   X-Ray Diffraction Theory 21
   2.4   Rietveld Refinement Theory 22
   2.5   Data Analysis 25
      2.5.1   Detector Calibration and Azimuthal Integrations 25
      2.5.2   Rietveld Refinement Using the FullProf Suite 26

CHAPTER 3   Results and Discussion 28
   3.1   Overview 28
   3.2   Undoped HA 28
      3.2.1   Refined Structural Parameters 28
      3.2.2   Thermal Evolution 29
   3.3   Zn-doped HA 34
      3.3.1   Refined Structural Parameters 34
      3.3.2   Thermal Evolution 35
   3.4   Sr-doped HA, Model I 47
      3.4.1   Refined Structural Parameters 47
      3.4.2   Thermal Evolution 47
   3.5   Theoretical Modeling 56

CHAPTER 4   Conclusions 57

Appendix 59

TABLE OF CONTENTS – *Continued*

LIST OF FIGURES

LIST OF FIGURES – *Continued*

LIST OF FIGURES – *Continued*

LIST OF FIGURES – *Continued*

LIST OF TABLES

ABSTRACT

Hydroxyapatite (HA) is a bioceramic that synthetically mimics human bone. It is commonly used in medical applications as a filler for damaged bone, and in procedures such as dental implants and hip replacements. Doping of HA with elements such as zinc and strontium is known to increase the bioactivity of HA, as well as increase the retention and adsorption of therapeutic molecules for drug delivery. High-temperature, *in-situ* X-ray diffraction data were measured on 10 at. % zinc-doped, 10 at. % strontium-doped, and undoped HA powders at the Advanced Photon Source at Argonne National Laboratory. This research studied the temporal and thermal evolution of these samples, which were prepared via wet synthesis. Two dimensional diffraction images were collected as the samples were heated from room temperature up to 800 °C. The crystallographic structures and phase transitions were determined from Rietveld analysis, using programs such as GSAS-II, the FullProf Suite, and Matlab scripts. The undoped HA powder remained single phase throughout the heating cycle. The zinc dopant greatly reduced the temperature for onset of decomposition into α- and β-tricalcium phosphate, which occurred at approximately 690 °C. The strontium-doped sample was more stable, but also exhibited a phase transition with decomposition into α-tricalcium phosphate occurring at 790 °C. Some applications prefer HA which is more biocompatible, while others prefer tricalcium phosphate which is more bioresorbable, *in-vivo*. It is then sometimes preferable to produce a biphasic material (HA + TCP) which can be obtained by high temperature annealing of Zn- and Sr-doped HA. In clinical applications, Zn and Sr doping amounts would be below 2 at. %, because higher levels could be toxic. Higher doping amounts reveal which phases form more quickly as a function of annealing temperature and provides important information about sample stability in general. Therefore these results provide useful insight on the optimization of

Zn- and Sr-doped HA materials for biomedical applications.

CHAPTER 1

Introduction

1.1   Background

The study of materials in environments other than ambient conditions is of increasing interest and importance in understanding structure-property relationships. This research focuses on the evolution of the crystal structure of hydroxyapatite in extreme high-temperature conditions. Understanding the stability of doped and undoped hydroxyapatite at high temperatures has direct correlations to understanding its stability within the human body. Certain phase changes may be induced at high temperatures, while those same phase changes, or different ones may arise due to conditions and interactions within the human body. Furthermore, bone implants and grafts are created from high-temperature sintering of hydroxyapatite powder.[1] It is important to know which phases form in doped HA, and what their effects would be *in-vivo*, if used for bone grafts. Therefore, structure-property relationships are especially important here in understanding the effectiveness of hydroxyapatite in medical applications. Hydroxyapatite is also a material of high interest because of its capture-release properties of cations important in biological processes, such as zinc and strontium.

To bolster understanding of the structural changes, and other potential applications of hydroxyapatite including those outside of the medical field, samples were heated from room temperature to 800 °C and cooled back down to room temperature. Throughout the experiment, phase transitions in the crystal structure were determined. Compared to the literature, differences in thermal evolution and stability are observed for zinc-doped HA in this research. However, this is most likely due to differences in sample preparation and processing among various studies, which alter inherent material properties. Understanding and monitoring studies similar to this

one are vital to optimization of doped HA for use as a bioceramic.

1.2   Crystallographic Structure

The structure of hydroxyapatite was first determined by Kay *et al.*, and the atomic positions are shown in Table 1.[2] Structurally, hydroxyapatite belongs to the hexagonal crystal system, $P6_3/m$ space group, and has unit cell dimensions $a = b = 9.432$ and $c = 6.881$ angstroms.[2] In crystallography, a, b, and c refer to unit cell edges. In three dimensions, a, b, and c are parallel to the x, y, and z axes, respectively. Fig. 1.1 is a top-view representation of the structure of hydroxyapatite, and Fig. 1.2 shows a rotated view to more clearly exhibit atomic positions. Forty-four atoms are found in one unit cell, as can be discerned from the hydroxyapatite unit formula, $Ca_{10}(PO_4)_6(OH)_2$.
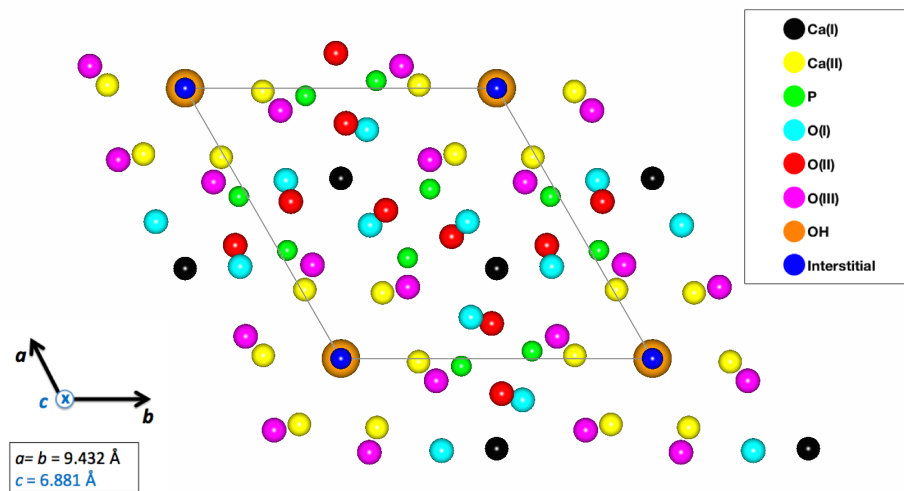
Figure 1.1: Top view of a hydroxyapatite unit cell showing Ca(I) and Ca(II) sites, with an interstitial site 2b. There is clear hexagonal positioning of Ca(II) and O(III).
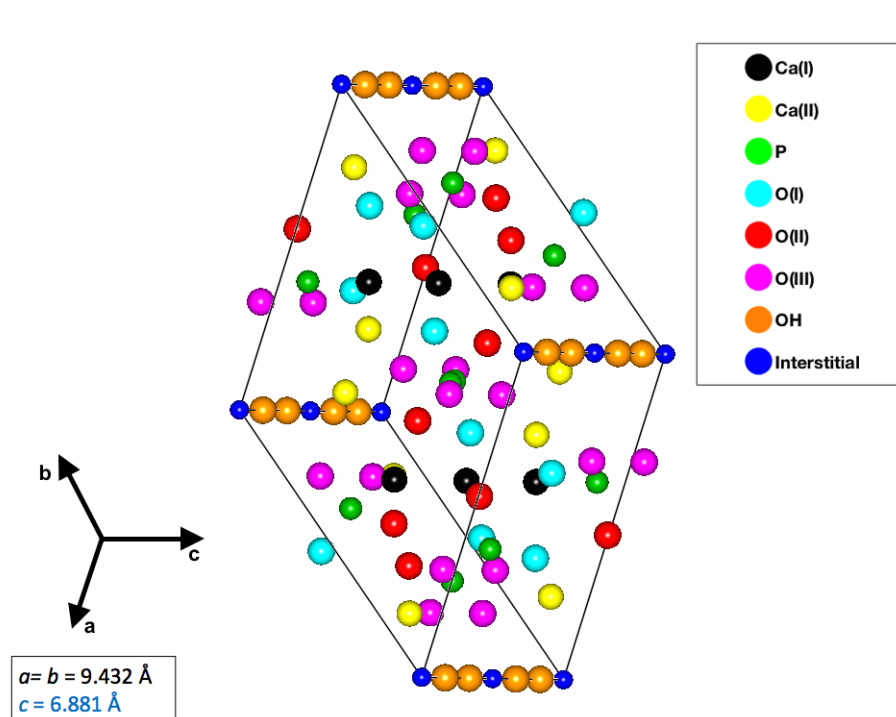
Figure 1.2: Rotated view of a hydroxyapatite unit cell showing Ca(I) and Ca(II) sites. The hydroxyl oxygen (OH), and interstitial site 2b positions are more clearly seen in this view.

Atoms	Positions	Wyckoff Letter	Maximum Occupation
Oxygen I		h	6
x	0.3283(2)		
y	0.4846(2)		
z	1/4		
Oxygen II		h	6
x	0.5876(2)		
y	0.4652(2)		
z	1/4		
Oxygen III		i	12
x	0.3433(1)		
y	0.2579(1)		
z	0.0705(2)		
Phosphorus		h	6
x	0.3982(2)		
y	0.3682(2)		
z	1/4		
Calcium I		f	4
x	1/3		
y	2/3		
z	0.0014(4)		
Calcium II		h	6
x	0.2466(2)		
y	0.9931(2)		
z	1/4		
Hydroxyl Oxygen (OH)		e	2
x	0		
y	0		
z	0.2008(7)		
Hydrogen		e	2
x	0		
y	0		
z	0.0617(15)		
Interstitial		b	2*
x	0		
y	0		
z	1/2		

Table 1.1: Atomic positions of the crystal structure of an undoped hydroxyapatite $(Ca_{10}(PO_4)_6(OH)_2)$ unit cell. The values in parentheses are uncertainties associated with the values of the last digit(s).*In pure HA, this 2b site has an occupation of zero, so it is considered an interstitial site. Adapted from Kay *et al.*[2]

1.3 Literature Review

Hydroxyapatite is most widely utilized in the field of medicine, mainly for bone grafts and for coating metallic implants. This section will provide a brief summary of zinc- and strontium-doped hydroxyapatite bioactivity, atomic behavior, as well as potential environmental applications. A survey of the effects of Zn and Sr dopants on the structure of HA will also be presented.

Numerous studies have been carried out on hydroxyapatite and other calcium phosphates, with cationic substitutions such as zinc, strontium, and magnesium.[3,4,5,6] Hydroxyapatite doping is done in order to more closely mimic the chemistry of pure bone, as well as for potential biological benefits.[1] Research on doping HA with zinc is relatively recent, and has produced various contradicting results. Furthermore, there are very few studies on the biological (*in-vivo*, and *in-vitro*) effect of zinc-doped HA. Nearly all zinc-doped HA studies show, however, that the zinc dopant displays inhibition of bone resorption, while serving as a good promoter of bone growth coupled with possible antibacterial effects.[1] Various metal-doped hydroxyapatites are also of high interest for their ability to capture and release metal ions that may have positive effects in HA bone dynamics.[7,8]

Theoretical modeling on zinc-doped HA suggests that the calcium II site is more energetically favorable than the calcium I site.[1,4] Various experiments report a discrepancy between the attempted amount of zinc substituted into their samples, and the actual amount of zinc that substitutes into HA. A study done on wet-synthesis, heat-treated zinc-doped HA by Miyaji *et al.*, for example, reports the differences in the "a" and "c" unit cell parameters for a range of zinc-doping amounts.[9] Miyaji *et al.* saw a decrease in lattice parameter "a" size for doping levels ranging from 0 to 5 mol%.[9] For samples with doping amounts between 5 and 10 mol%, presumed incorporation of water (H_2O) into the HA lattice structure resulted in a consistent increase of lattice parameter "a", before leveling off for samples with doping levels higher than 10 mol%. Heat treatment of these samples up to 400 °C was sufficient in inhibiting water effects on the HA structure, and resulted in the expected decrease

of "a" as a function of chemical composition (mol%).[9] The expected result is due to an increased amount of Zn^{2+}, which has a smaller ionic radius than Ca^{2+}, in the HA structure. Bigi *et al.* conducted a wet synthesis zinc-doped HA experiment, and reported that zinc cannot significantly substitute for calcium in the HA structure.[10] Rather, it was concluded that zinc inhibits crystallization of HA, and is most highly concentrated either on the HA surface, or in the amorphous β-TCP phase.[10] Mayer and Featherstone, however, reported successful substitution of zinc in carbonated HA samples for a range of doping levels.[11]

Gomes *et al.* reported the results of an *ex-situ* X-ray diffraction experiment involving zinc-doped biphasic calcium phosphate (BCP), with samples subjected to a heating cycle peaking at 1100 °C prior to the diffraction measurements.[3] BCP is a mixture of hydroxyapatite and β-tricalcium phosphate ($Ca_3O_8P_2$, abbreviated as TCP) whose presence is induced by the zinc dopant. Contrary to results by Matsunaga *et al.*[4], Gomes *et al.*[3] found that there was no preference for zinc substitution in the Ca II site. In fact, they reported that zinc was only present in the interstitial 2b site, and that sites I and II were composed of 100% calcium.[3,4] After heat treatment, three phases were present in the 10 zinc atomic percent sample ($Ca_{10-x}Zn_x(PO_4)_6(OH)_2$, where $x = 1$): hydroxyapatite, β-TCP, and ZnO. They also found that the zinc dopant had little effect on the unit cell volume. It is important to note that the samples in that experiment were not run *in-situ*. The samples were prepared, heat treated for 15 hours, quenched, and then diffraction data were collected at room temperature. The samples were synthesized via the sol-gel process, where a liquid solution undergoes a transition into a rigid gel via addition of solid nanoparticles. The gel was heated for ten hours at 80 °C to obtain a powder.[3]

Similar to ZnHA, strontium-doped HA samples have shown increased osteoblast production *in-vivo*, while inhibiting the activity of osteoclasts that cause bone resorption.[1] In strontium-doped HA experiments, strontium was found to substitute into both the Ca I and Ca II sites. Similarly to zinc-doped HA, but with more consistent results, the preferred site for strontium substitution is the Ca II site.[1,5,12,13] Bigi *et al.*[12], however, found no preferred substitution site for samples

with low strontium weights, while Terra *et al.*[5] found that strontium preferred substitution in site I for samples with Sr concentrations 1 at. %, but site II was preferred for concentrations of 10 and 15.

Hydroxyapatite also has environmental applications. Kottegoda *et al.* describes the use of hydroxyapatite nanoparticles with urea, a nitrogeneous and water-soluble plant nutrient, surface modifications in order for soil to better utilize nitrogen.[14] Noted as an invaluable resource in food, biomass, and fiber production, nitrogen is a highly important component in fertilizers.[14] Due to leaching, however, over half of the nitrogen put into fertilizers is lost to the soil. This means that more fertilizer is needed, and thus a higher expense incurred in order to get plants necessary amounts of nitrogen. Kottegoda *et al.* reported the use of urea-modified hydroxyapatite nanoparticles encapsulated in soft wood, for slow release of nitrogen into fertilizer. Another study by Sneddon *et al.* reports the use of hydroxyapatite in the form of bone meal, as a means of metal immobilization in contaminated soils (above-neutral pH).[15] The presence of metals in soil is potentially hazardous to humans and the environment, if released into soil solution.[15] Sneddon *et al.* reported that, over 18 months the introduction of hydroxyapatite bone meal formed low-solubility metal phosphates with lead, zinc, and cadmium present in the soil. These findings indicate that bone meal could be a highly effective material in the reduction of metal mobility, bioavailability in ground and surface waters.

1.4   Motivation for this Study

This research specifically aims to understand the overall stability of hydroxyapatite, and to determine phase changes that take place within the undoped, zinc-doped, and strontium-doped samples. Synchrotron X-ray diffraction data were collected *in-situ*, from room temperature up to 800 °C using 2D detectors. The data were analyzed with the Rietveld method (section 2.4) in order to obtain structural information about the samples and the evolution of crystallographic phases. To this end, comparison of sample stabilities with related studies is important in determining the

optimal combination of sample preparation and doping amount for specific functions. The research on doped HA was done specifically on samples with a 10 at. % doping amount: $Ca_{10-x}Zn_x(PO_4)_6(OH)_2$, where $x = 1$, and $Ca_{10-x}Sr_x(PO_4)_6(OH)_2$, where $x = 1$ as well.

CHAPTER 2

Experimental Procedure

2.1   Sample Preparation

Samples were prepared by the Rossi group in Brazil via wet-synthesis. The following describes the preparation of the ZnHA sample and the SrHA sample. Zinc-doped hydroxyapatite, $Ca_{10-x}Zn_x(PO_4)_6(OH)_2$, where $x = 1.0$, was precipitated via addition of an aqueous solution containing $Ca(NO_3)_2$, and $Zn(NO_3)_2$ to a $(NH_4)_2HPO_4$ solution. The aqueous solution was added at a flow rate of 5 ml/min at a temperature of 90 °C with pH $= 9.0$.[1] At this point, the solution was a heterogeneous mixture, and was stirred for three hours at the same temperature. The precipitate was separated through a filtration process, frequently washed with boiling, deionized water, and dried at 100 °C. Finally, the precipitate was manually ground and sieved into a uniform powder.[8]

Strontium-doped HA, $Ca_{10-x}Sr_x(PO_4)_6(OH)_2$ (where $x = 1$), was precipitated in a similar fashion to ZnHA. In a dropwise manner, an aqueous solution of calcium nitrate $Ca(NO_3)_2$, and $Sr(NO_3)_2$ was added to a $(NH_4)_2HPO_4$ solution at a flow rate of 5 ml/min and temperature of 90 °C. A solution pH of 10.0 was preserved by addition of NH_4OH. The precipitate was treated in the same manner as the ZnHA precipitate, and then ground and sieved into a uniform powder.[5] Undoped HA, $Ca_{10}(PO_4)_6(OH)_2$, was prepared using the same procedure as the doped samples, with the exclusion of the metal nitrates $(Zn(NO_3)_2$, and $Sr(NO_3)_2)$.

2.2   X-ray Diffraction Measurements

X-ray diffraction data on the three powder samples were collected at Sector 1 (1-BM-C beamline) of the Advanced Photon Source at Argonne National Laboratory.

Each batch of hydroxyapatite powder was loaded into a capillary, which was placed into a high-temperature flow cell/furnace utilized for *in-situ* studies of materials under non-ambient conditions.[16] This versatile furnace allows for accessible control of environmental parameters. Within the capillary, gas, vapor, and fluid environments can be varied under static or flow conditions at varying pressures. In this experiment, ultra-high purity oxygen was allowed to flow through the capillary. The extruded quartz glass capillary used in this experiment had a diameter of 0.9 mm. Quartz capillaries remain amorphous below 853 °C, which was very suitable for this experiment, where temperatures peaked at 800 °C. X-ray diffraction images were collected every two minutes. The controlled temperature profile for the experiment can be seen in Fig 2.1. Annealing temperature was held constant for approximately one hour at 120 °C, and 800 °C. The constant temperature of 120 °C correlates to the absorption of surface water. The sample was held at 800 °C in order to investigate any changes in the relative amount of phases and if any new phases formed at that temperature. It was estimated that one hour at 120 °C was sufficient for complete evaporation of surface water. To be consistent, the sample was held at maximum temperature for the same amount of time.

The incident x-ray beam was set to an energy of 20.27 keV. The beam size was 300 microns in diameter. For zinc-doped and undoped hydroxyapatite, 250 two-dimensional diffraction images were measured. Five hundred diffraction images were taken for the strontium-doped hydroxyapatite sample, because an extra 250 measurements were taken while the sample was cooled to room temperature. Throughout these extra measurements, there was only a very slight temperature variation (28 °C to 26 °C). Diffraction data were collected using a Perkin-Elmer XRD 1621 area detector. The detector has a total area of 409.6 x 409.6 mm^2, with a 2048 x 2048 array at 200 μm pixel pitch.
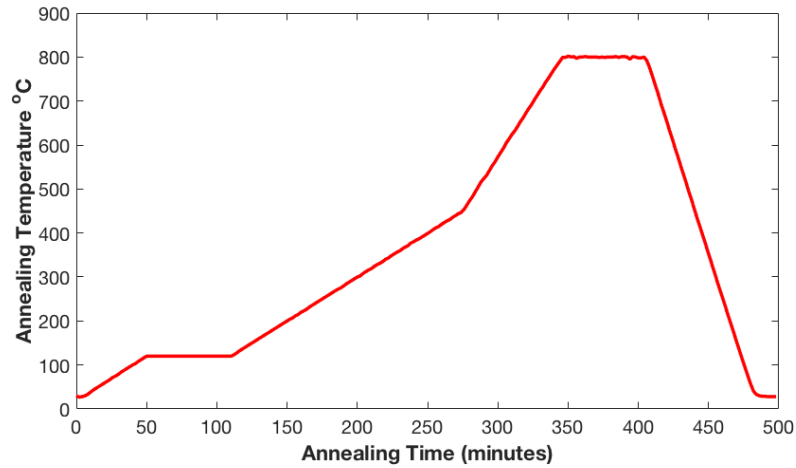
Figure 2.1: The controlled temperature cycle used for all three hydroxyapatite samples.

2.3   X-Ray Diffraction Theory

In order to understand the physical properties of a material, its atomic structure must be discerned. Measured intensities of X-ray diffraction data contain structural information about a given sample. Diffraction peak intensity depends on electron density, which is in turn a function of atomic positions within the unit cells of any crystalline sample. Diffraction occurs if a beam of X-rays incident on a sample at an angle of θ satisfies Bragg's law,

$$m\lambda = 2dsin\theta \tag{2.1}$$

In the equation above, m is a positive integer, λ is the wavelength of the incident X-ray, θ is the angle of incidence of the incoming X-ray with respect to the crystal surface, and d is the spacing between atomic planes in the crystal lattice. Diffraction rings with defined 2θ angles represent regions of constructive interference (see section 2.5.1). The angle 2θ is the angle between the transmitted incident X-ray beam, and the detector. X-ray diffraction images and patterns are thus shown as a function of 2θ, where θ is the angle that satisfies Bragg's Law. In an X-ray diffraction pattern, the intensity of diffraction peaks are related to the electron density (atomic arrangement) within a crystal. Intensity is proportional to the structure factor,

$F_{h,k,l}$ of a material,

$$I_{h,k,l} \propto |F_{h,k,l}|^2 \tag{2.2}$$

The structure factor is given by,

$$F_{h,k,l} = \sum_{j=1}^{n} f_j exp\big[2\pi i(hx_j + ky_j + lz_j)\big] \tag{2.3}$$

where f_j is an individual atomic scattering factor corresponding to the efficiency of X-ray scattering at any angle due to the electron density within an atom. The location of atoms on certain atomic planes is described by x_j, y_j, and z_j. The structure factor describes how a material scatters incident radiation by summing the result of scattering from all atoms in a unit cell. With this information, the structure factor reveals which reflections (hkl) are observed in a diffraction pattern. Diffraction patterns, therefore, correlate directly to atomic structure.

2.4   Rietveld Refinement Theory

In 1967, H.M. Rietveld developed a structure refinement procedure that uses a least-squares fit between calculated and observed intensities for powder diffraction patterns.[18,19] This method is much more reliable than the previous practice of using the integrated intensities of overlapping peaks. Rietveld refinement is so effective because it utilizes all available information from an entire diffraction pattern, including relationships between peak shape, width, and position, to obtain the best possible value for intensities. Through this method, a powder diffraction pattern can yield quantitative structural information.

Originally, Rietveld developed this structure refinement method for neutron diffraction data, modeling peaks in a diffraction profile with a Gaussian function,

$$Y_{i,k} = tS_k^2 j_k L_k \frac{2\sqrt{ln2}}{H_k\sqrt{\pi}} \exp\left[\frac{-4ln(2)}{H_k^2}(2\theta_i - 2\theta_k)^2\right] \tag{2.4}$$

where $Y_{i,k}$ is the intensity at point i due to reflection k, t is the step width of the diffractometer, S_k^2 is the sum of the nuclear and magnetic structure factors, j_k is

the multiplicity of reflection k, L_k is the Lorentz factor, $2\theta_k$ is the calculated Bragg angle of reflection k, $2\theta_i$ the Bragg angle at point i, and H_k is the full width at half maximum (FWHM) for reflection k. In a diffraction pattern, the FWHM of diffraction peaks is not constant, and the angular dependence is given by,

$$H_k^2 = U tan^2\theta_k + V tan\theta_k + W \tag{2.5}$$

where U, V, and W are halfwidth parameters.[19]

This function is the basis for all peak-fitting models of diffraction data. However, X-ray diffraction data in particular are usually modeled with a pseudo-Voigt function, rather than a Gaussian. In general, a pseudo-Voigt function is a combination of Gaussian and Lorentzian functions, and all modeling functions contain the variable H_k. A brief description of the Rietveld method is given below, and all equations are adapted from Rodríguez-Carvajal.[20]

Data are numerically recorded for a discrete set of 2θ scattering angles, which will be referred to as scattering variable T. The calculated profile intensity given at a certain ith step along the scattering variable is given by,

$$y_{c,i} = b_i + \sum_\phi S_\phi \sum_h I_{\phi,h}\Omega(T_i - T_{\phi,h}) \tag{2.6}$$

The vector h corresponds to the Bragg reflections that contribute to the ith point in the scattering variable. The phase, ϕ, varies from 1 to the number of crystallographic phases that exist in the sample. For example, in zinc-doped hydroxyapatite, more phases form as the temperature of the sample is increased. The scale factor of the phase is denoted as S_ϕ. The reflection profile function, Ω, contains instrumental and sample effects. The background intensity is denoted as b_i. The expression for the integrated intensity, $I_{\phi,h}$, is defined as,

$$I_{\phi,h} = \left[LAPCF^2\right]_{\phi,h} \tag{2.7}$$

The term L_h contains Lorentz polarization and multiplicity factors. The structure factor of the sample is denoted as $F_{\phi,h}$. Absorption corrections in XRD (X-ray

Diffraction) data is denoted as A_h. The preferred orientation function for the sample is given by P_h, while C_h contains special corrections for absorption, extinctions, etc. More specifically, the Rietveld method consists of minimizing the weighted-square difference between the calculated and observed peak intensities. This function is referred to as the chi-squared function, and the goodness of fit of the diffraction data is dictated by the minimization of this function,

$$\chi^2 = \sum_{i=1}^{n} w_i [y_i - y_{c,i}(\alpha)]^2 \tag{2.8}$$

where w_i is defined as $\frac{1}{\sigma_i^2}$, and σ_i^2 is the variance of the observation "y_i". The closer this function is to one, the better the fit in the data profile refinement. FullProf calculates the reduced chi-squared,

$$\chi_r^2 = \left[\frac{R_{wp}}{R_{exp}} \right]^2 \tag{2.9}$$

The terms, R_{wp} and R_{exp} are the weighted profile factor, and the expected weighted profile factor, respectively. The ratio of these two is the goodness of fit indicator. Their respective equations are,

$$R_{wp} = 100 \left[\frac{\sum\limits_{i=l,n} w_i |y_i - y_{c,i}|^2}{\sum\limits_{i=l,n} w_i y_i^2} \right]^{\frac{1}{2}} \tag{2.10}$$

and,

$$R_{exp} = 100 \left[\frac{n - p}{\sum\limits_{i} w_i y_i^2} \right]^{\frac{1}{2}} \tag{2.11}$$

where $n - p$ denotes the number of degrees of freedom. The variable n is the total number of points in a diffraction pattern, minus the total number of excluded points. The variable p is the number of refined parameters.

The Bragg factor, R_B, is another function used to determine "goodness of fit," and is given by,

$$R_B = 100 \frac{\sum_h |I_{obs,h} - I_{calc,h}|}{\sum_h |I_{obs,h}|} \tag{2.12}$$

In the above equation, $I_{calc,h}$ is the calculated integrated intensity, while $I_{obs,h}$ is the observed integrated intensity, both integrated over a specific 2θ range. Comparatively, $y_{c,i}$ (see above) is the calculated non-integrated profile intensity, while y_i is the observed non-integrated profile intensity. Observed intensities correspond to the raw X-ray diffraction data measured during the experiment. The calculated values correspond to the best possible crystallographic model (pseudo-Voigt) to fit the data, as will be discussed below in section 2.5.2.

2.5 Data Analysis

2.5.1 Detector Calibration and Azimuthal Integrations

GSAS-II is a software package developed at Argonne National Laboratory that expedites crystallographic calculations, data reduction, and allows for structure refinement and determination.[17] GSAS-II was utilized to calibrate the Perkin-Elmer area detector used in the experiment, in order to map each pixel to a known 2θ and azimuth angle. Detector calibration is performed by measuring diffraction data from a standard powder obtained from NIST (National Institute of Standards and Technology). From this measurement, experimental parameters, such as sample-to-detector distance, tilt angles between the normal of the detector and the X-ray beam, and the exact energy of the photons were determined. GSAS-II was then used to integrate the data. A range of azimuthal 2θ angles between $3°$ and $34°$ were used in the integrations, in order to remove an absorption effect in the images arising from the beamstop holder, as shown in Fig. 2.2. Using the 660a LaB_6 NIST calibration standard, the sample-to-detector distance was determined to be 330 mm, and the X-ray energy was 20.27 keV. After the proper calibration was performed, the 2D images were azimuthally integrated to obtain powder files of intensity vs. scattering angle (2θ). The GSAS-II diffraction files were formatted with Matlab

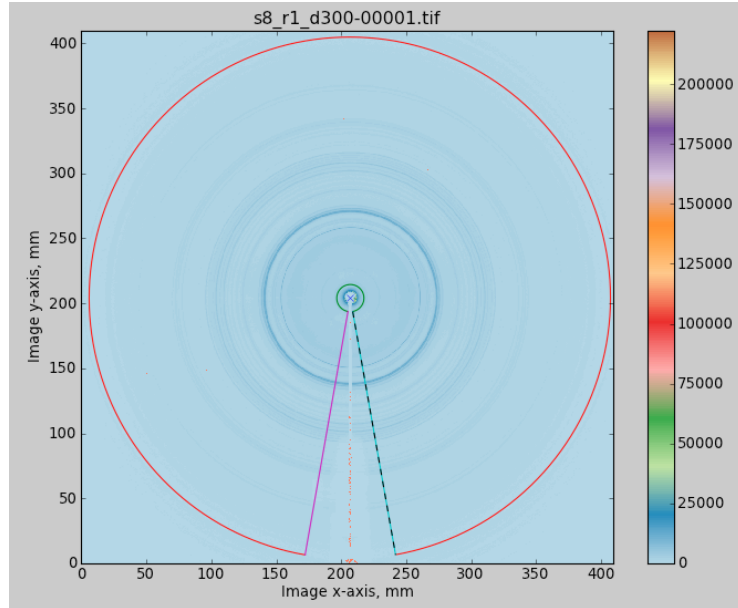scripts to perform Rietveld analysis using the FullProf Suite software.

Figure 2.2: An example of a diffraction image in GSAS-II, with the limits of integration excluding the region of absorption due to the beamstop holder. The thickness of the Debye rings correspond to peak widths in an integrated powder XRD pattern.

2.5.2   Rietveld Refinement Using the FullProf Suite

FullProf is a program developed and utilized mainly for Rietveld analysis (structure profile refinement) of X-ray and neutron diffraction data. As discussed in section 2.4 in detail, the Rietveld method takes a specific set of crystallographic data and finds the best possible model to fit that data. Specifically, a space group, atomic positions, lattice parameters, profile parameters, specific X-ray wavelength, and the resolution function obtained from the calibration standard have to be given to FullProf. Then, the parameters to be refined are specified, and FullProf performs a least-squares fitting to find the best possible crystallographic model for the data. During the refinements of all three samples, it was observed that the intensities of the diffraction peaks were not fitted properly if an isotropic grain size (*i.e.*, spherical) was

assumed. A grain shape model that uses spherical harmonics was then implemented by FullProf to account for size anisotropy.[21] Both structural and microstructural refined parameters and their uncertainties were obtained from output files generated by FullProf. These refined parameters and their uncertainties were then extracted using Matlab scripts.

CHAPTER 3

Results and Discussion

3.1 Overview

This chapter will discuss in detail the data that was analyzed for undoped, zinc-doped, and strontium-doped HA. Any phase transitions present in the samples through heating will be discussed. The behavior of individual HA unit cells, and HA powder grains will be discussed for each sample. As discussed in section 1.2, hydroxyapatite crystallizes in the hexagonal structure, where the crystallographic axes $a=b\neq c$. The expansion and contraction of lattice parameters a and c will be discussed. It is important to note that a single grain contains multiple unit cells, and for isotropic spherical powders, grains have random orientations. As mentioned earlier, a grain shape model using spherical harmonics was implemented by FullProf to account for size anisotropy. It was discerned that grain shapes were not spherical, rather they were needle-like. The Rietveld software calculates the apparent size for each individual measured diffraction peak. The deviation from spherical shape is then quantified by an anisotropy parameter, which corresponds to the standard deviation in the apparent size of all measured directions.

3.2 Undoped HA

3.2.1 Refined Structural Parameters

Since the chemical formula for undoped HA is $Ca_{10}(PO_4)_6(OH)_2$, the total occupation of the calcium sites in stoichiometric HA is given by Ca I + Ca II = 10. The crystallographic data from section 1.2, including the atomic positions in Table 1.1, were input in Fullprof, and parameters to be refined were specified. Subsequently, FullProf performed a least-squares fitting to find the best possible crystallographic

model (fit) for the raw data. For undoped HA, the refined structural parameters included: unit cell "a" and "c" parameters, the atomic positions (initial values are shown in Table 1.1), and the calcium occupancies. Because at room temperature, the occupancies refined to 4 and 6 for calcium I and II, respectively, these were fixed throughout the heating and cooling cycle of the experiment.

3.2.2 Thermal Evolution

Undoped HA remained single phase throughout the experiment. As can be seen in Figs 3.1 and 3.2, water evaporated and caused a non-linear volume and lattice expansions up to 300°C. The deviation from linearity was more pronounced in the "a" parameter than in the "c" parameter, as seen in Figure 3.2. The cooling of the sample showed a linear decrease in unit cell volume, "a", and "c" parameters.

The mean size of the grains, obtained from Rietveld refinement of 170 crystallographic reflections, is shown in Fig. 3.3, and the anisotropy in this mean size is plotted in Fig. 3.4. A grain consists of multiple hydroxyapatite unit cells that align themselves in three dimensions. As mentioned before, FullProf quantifies a deviation from spherical shape with an anisotropy parameter, which corresponds to the standard deviation in the apparent grain size using the 170 measured reflections. A high anisotropy denotes that the growth of the powder grains has a directional dependence, and that grain shapes deviate from a spherical shape (no anisotropy). Apparent size in the direction of two (out of 170) specific atomic planes are shown in Figs. 3.5 and 3.6. With a much higher than average size, the <001> atomic planes govern the anisotropy of the sample as a whole. This indicates that the grains are needle-shaped with a preferred orientation along the <001> planes. The grains thus grow preferentially along their c axes through heating, as shown in Fig. 3.7.

Uncertainties in refined structural parameters are given by Rietveld refinement of the data in FullProf. Lower uncertainties correspond to a better fitting of the XRD intensity data with the refined structural model, and also correlate with higher collection statistics. Uncertainties in the size data were calculated using error propagation of the size parameters with the largest uncertainties.
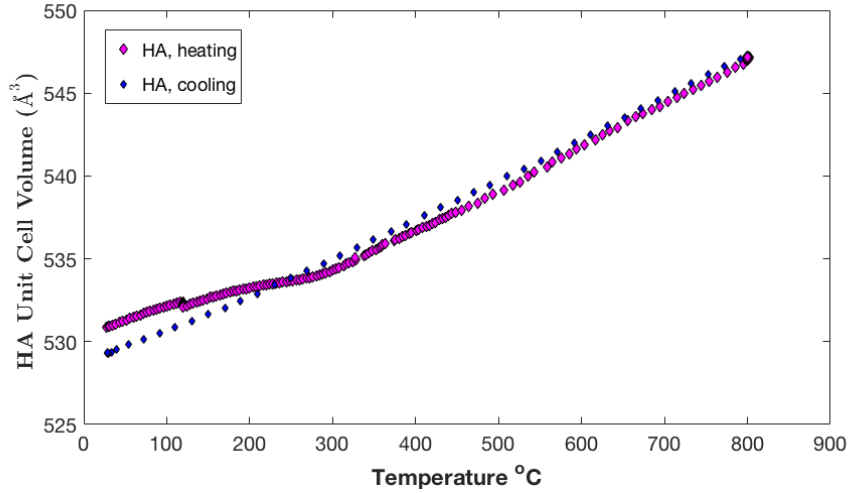
Figure 3.1: Undoped HA unit cell volume through heating, and cooling of the sample. The evaporation of water in the sample causes a non-linear expansion until approximately 300 °C. Cooling of the sample shows a linear decrease in unit cell volume.
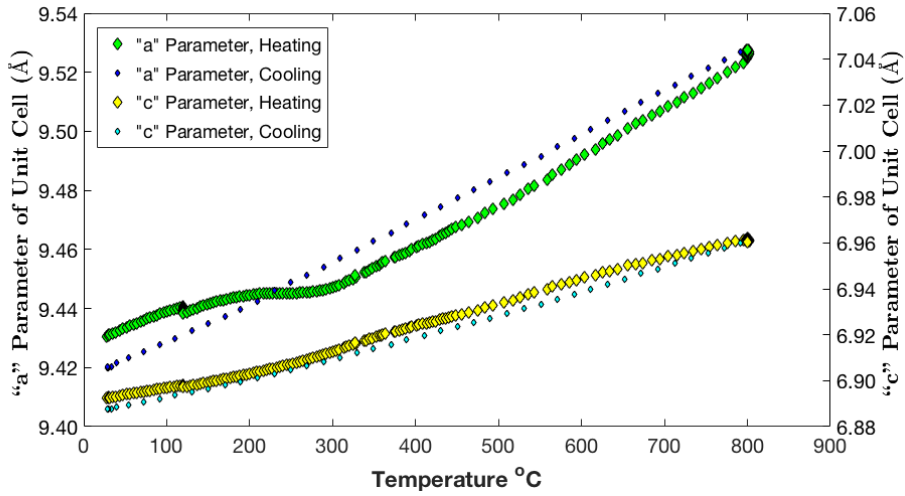

Figure 3.2: "a" and "c" parameters of undoped HA unit cell through heating, and cooling of the sample. The evaporation of water has a more significant effect on the thermal evolution of the "a" parameter, than the "c" parameter. Cooling shows a linear decrease in the size of both "a" and "c".
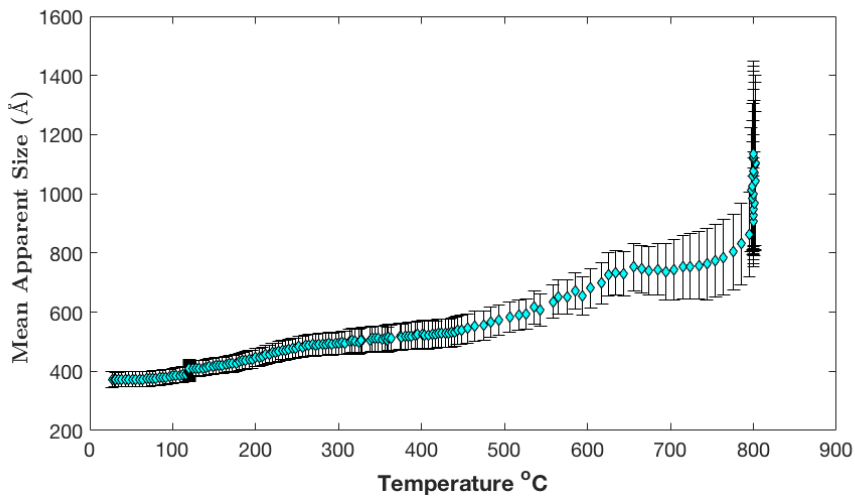
Figure 3.3: Mean apparent grain size of the undoped HA sample through the heating cycle.
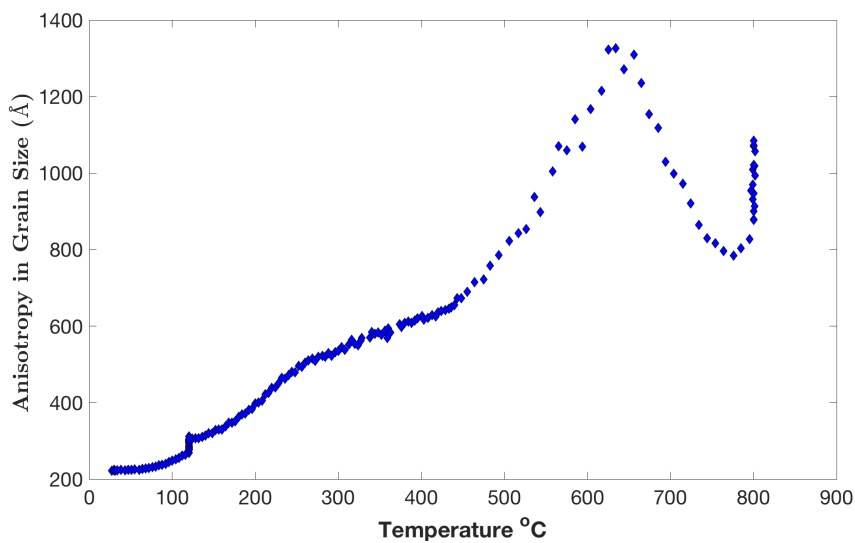

Figure 3.4: Anisotropy in the grain size of undoped HA. The anisotropy is the standard deviation of the apparent sizes obtained from the 170 measured reflections. The increase in anisotropy correlates to the grains' directional dependence, and preference during growth.
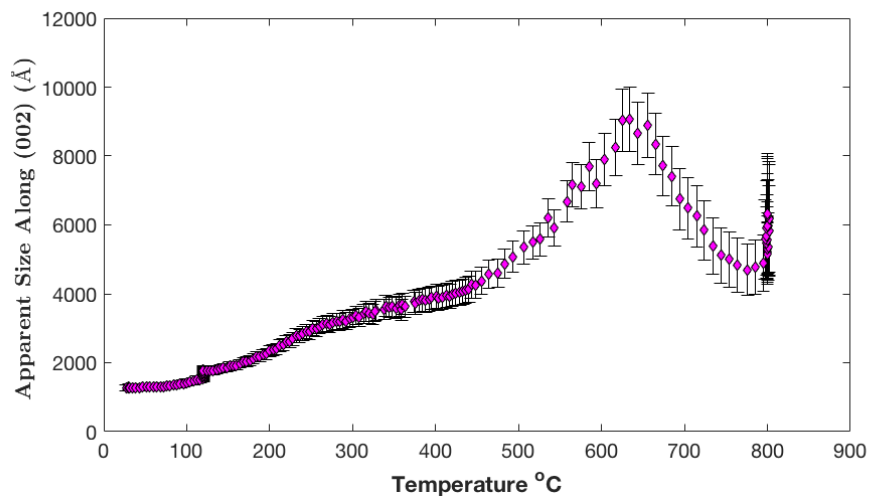
Figure 3.5: Undoped HA apparent size in the direction of (002) atomic planes throughout heating. The behavior of the growth along (002) affects the anisotropy in the mean apparent size, as seen in Fig. 3.4.
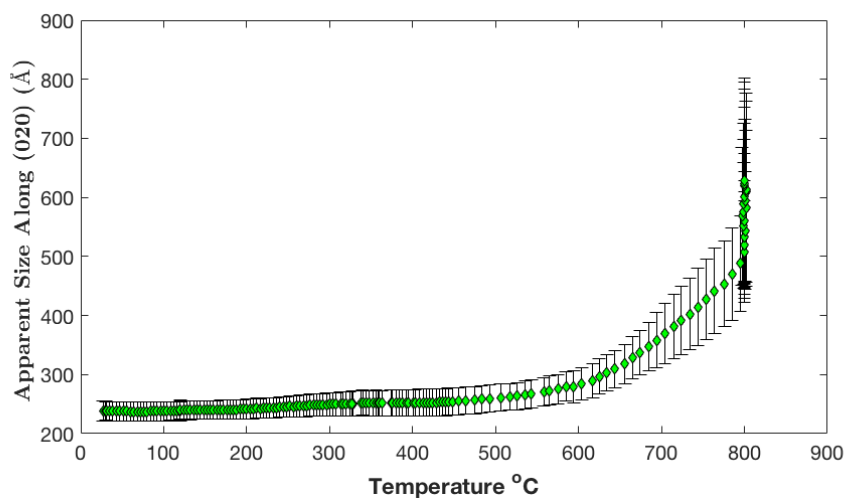

Figure 3.6: Undoped HA apparent size in the direction of (020) atomic planes throughout heating.
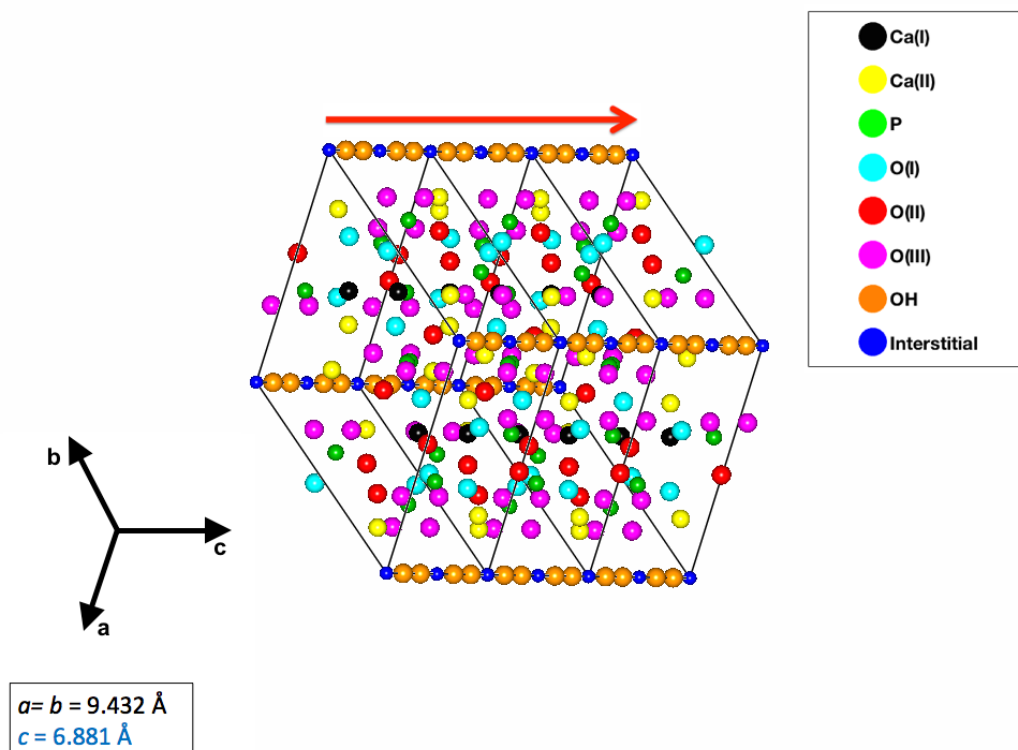
Figure 3.7: Hydroxyapatite unit cells aligned along the $< 001 >$ planes. Grain growth predominantly takes place along this direction through heating, exhibiting preferred orientation, and thus governing the anisotropy in grain shape.

3.3 Zn-doped HA

3.3.1 Refined Structural Parameters

For zinc-doped HA, the refined structural parameters included: unit cell "a" and "c" parameters, the atomic positions (initial values are shown in Table 1.1), the calcium and zinc occupancies at the Ca I and Ca II sites, and the occupation of zinc at interstitial site 2b. The inclusion of zinc at the interstitial 2b site in the refinements resulted in an improved fit of the diffraction data (lower chi-squared) in FullProf. Different refinement scenarios were explored to obtain the total amount of zinc and calcium in the sample. The refined total zinc ranged from 0.8 to 1.2 atoms per unit cell, with 1.0 giving the best fit. Because of the stoichiometry of the ZnHA sample, $(Ca_{10-x}Zn_x(PO_4)_6(OH)_2$, where $x = 1)$, it was expected that Ca I + Ca II = 9. However, it was found that by fixing Ca I + Ca II = 8.8, the chi-squared in the fit was further minimized.

Different scenarios of the combined calcium site occupations (Ca I + Ca II) ranging from 8.7 to 9.2 were investigated. The chi-squared values for these scenarios, showed a clear preference for Ca I + Ca II < 9, with 8.8 giving the best fit. Therefore, the total amount of zinc in the sample was fixed to Zn I + Zn II + $Zn_{interstitial}$ = 1.0, while the total calcium was fixed to 8.8. Since Ca I + Ca II = 8.8 < 9.0 produces the best fit, it can be discerned that for the zinc-doped samples, cation vacancies exist in these sites. Other refinement scenarios are currently being explored.

3.3.2 Thermal Evolution

Decomposition

The zinc-doped HA sample was less stable compared to undoped HA, and it started to decompose at approximately 690 °C into α-TCP, β-TCP, and ZnO, as shown in Fig. 3.8. By the end of the experiment, the vast majority of the sample had decomposed into β-TCP. The presence of β-TCP was surprising at such low temperatures. Even more interesting was the inclusion of the α-TCP phase, since its presence is sparsely seen in the literature. The very beginning of the cooling cycle can be seen in Fig. 3.8 , specifically for α- and β-TCP. It is likely that if the heating cycle had been longer, the trends in sample decomposition would have continued.
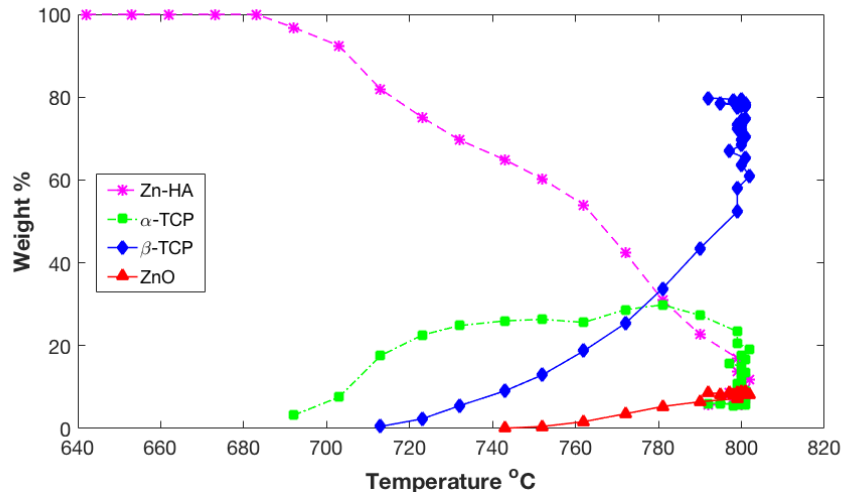

Figure 3.8: The fraction of ZnHA and decomposition phases (HA, α-TCP, β-TCP, and ZnO) *vs.* heating temperature.

Occupations of Cation Sites I and II

Figure 3.9 shows that there is a clear preference for zinc substitution in the Ca II site. While being consistent with most of the literature, the preference is more pronounced than in the majority of those studies. On average, approximately 65% percent of zinc in the sample occupied site II, while 34% occupied site I, and less

than 1% occupied the interstitial site. Considering the maximum occupancies of these sites, the Zn fractional occupations of sites I, II, and 2b are: 8.5%, 10.8%, and 3.5%, respectively. An increase in zinc occupation of site II, as well as an increase in the occupation of site I was observed to occur until approximately 350 °C. After this temperature, slight decreases occurred within each site, also shown in Fig. 3.9. The behavior and occupation of calcium in site I and site II are seen in Fig. 3.10. An initial increase of calcium in site II occurred, with a corresponding decrease of calcium in site I, before both sites remained relatively stable in calcium occupancies. The combined zinc and calcium occupations of site I and site II are shown in Fig. 3.11. Here, the presence of vacancies is seen, since a fully occupied site I would have 4 atoms per unit cell, while a fully occupied site II would have 6 atoms. Site I has a greater amount of vacancies than site II.
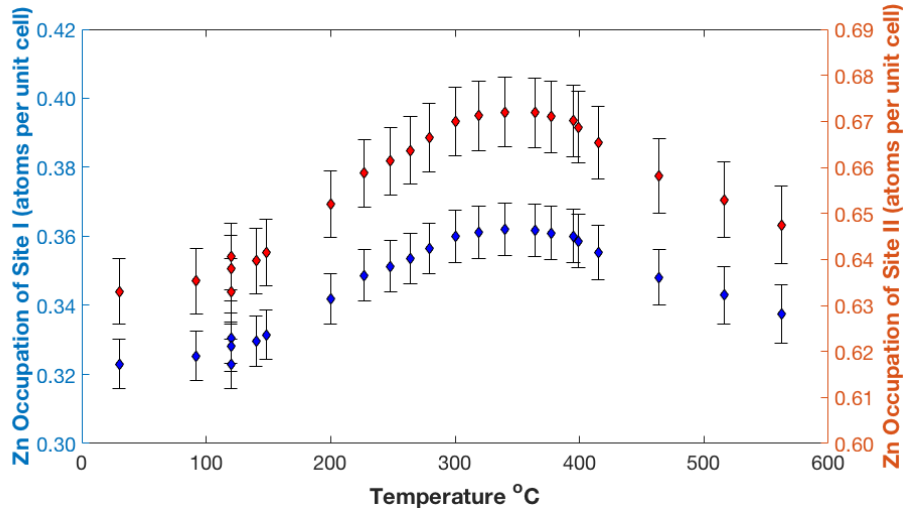

Figure 3.9: Zinc occupation of cation site I and site II. Site II is the preferred substitution site for zinc.
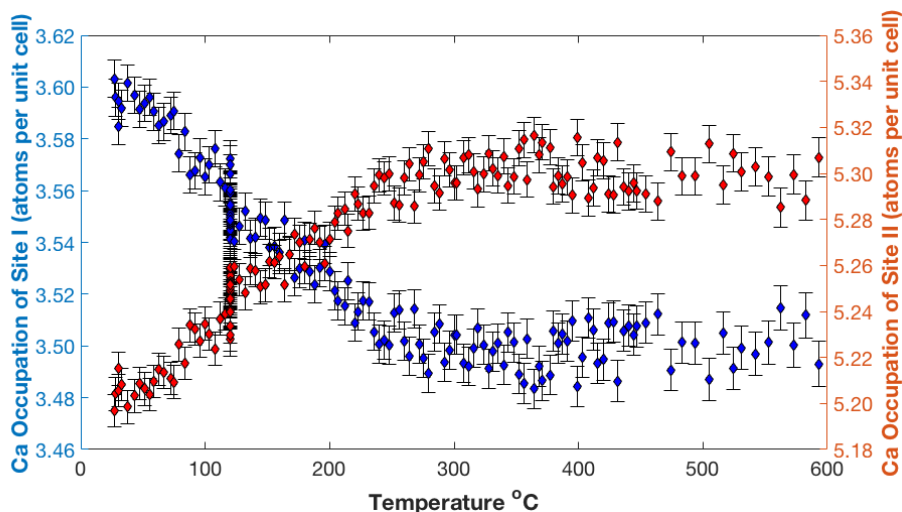
Figure 3.10: Calcium occupations of site I and site II within the HA unit cell. Calcium occupancies in each site remain relatively stable past 300 °C.
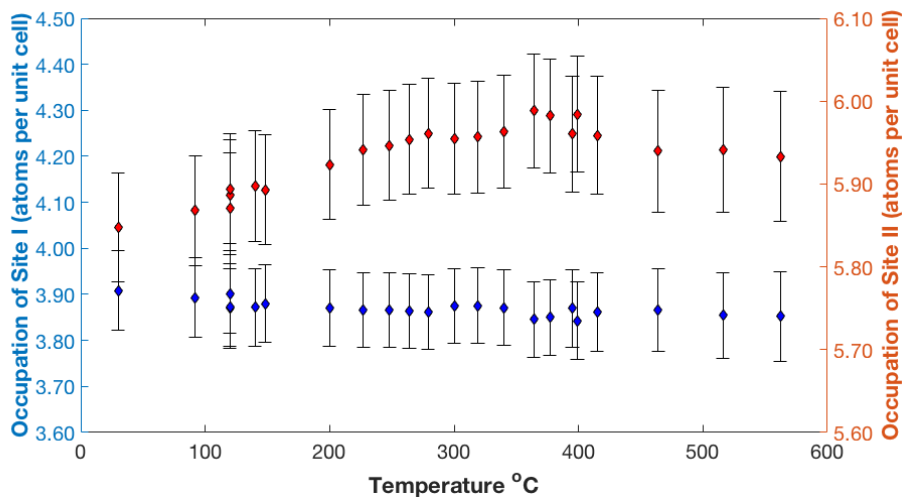

Figure 3.11: Total occupation (zinc + calcium) for site I and site II. A fully occupied site I would have 4 atoms, while a fully occupied site II would have 6. Neither site is fully occupied, meaning that vacancies are present in the sample.

Occupation of the 2b Interstitial Site

Proper fitting of the (010) reflection with a special asymmetric correction affected the calculated amount of zinc present in the interstitial site. Fig. 3.12 shows a Rietveld refinement for the ZnHa sample at 30°C. Only one phase is present, and the (010) and (002) peaks are labeled. Fig. 3.13 shows the (010) reflection more clearly, and compares the Rietveld fit of the peak with and without the asymmetric correction. The behavior of zinc in interstitial site 2b throughout heat treatment is shown in Fig. 3.14. The initial decrease in zinc occupation of this site corresponds to an increase of zinc occupation in both site I and site II. Similarly, the increase in zinc occupation of this interstitial site is coupled with a slight decrease in occupation of both sites I and II. The presence of zinc interstitials correlates to non-linear volume changes (shown in the following section), removal of surface (around 100 °C) and crystalline water (up to 350 °C), and cation vacancies, all in agreement with complex defects predicted by theoretical simulations.[8]
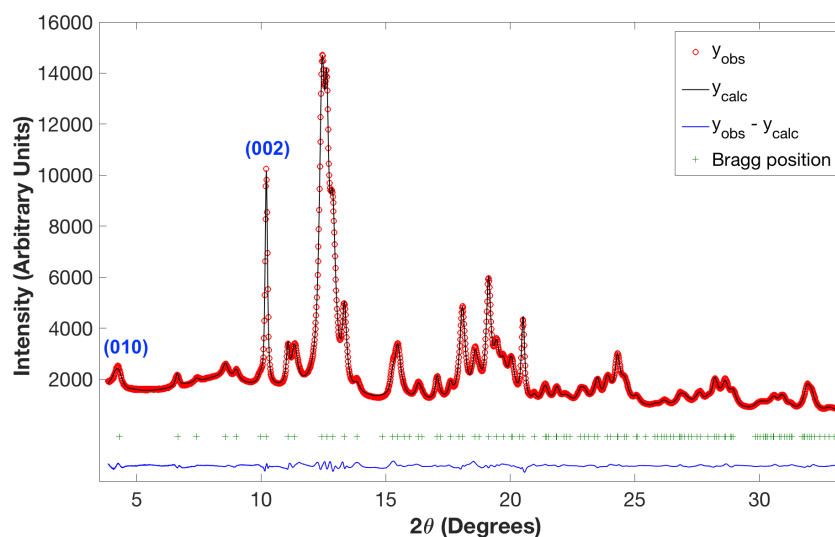

Figure 3.12: An example of a Rietveld fit in FullProf for the first ZnHA data file (single phase). For this data file, the χ^2 value is 1.50, and the R_{Bragg} factor is 1.565.
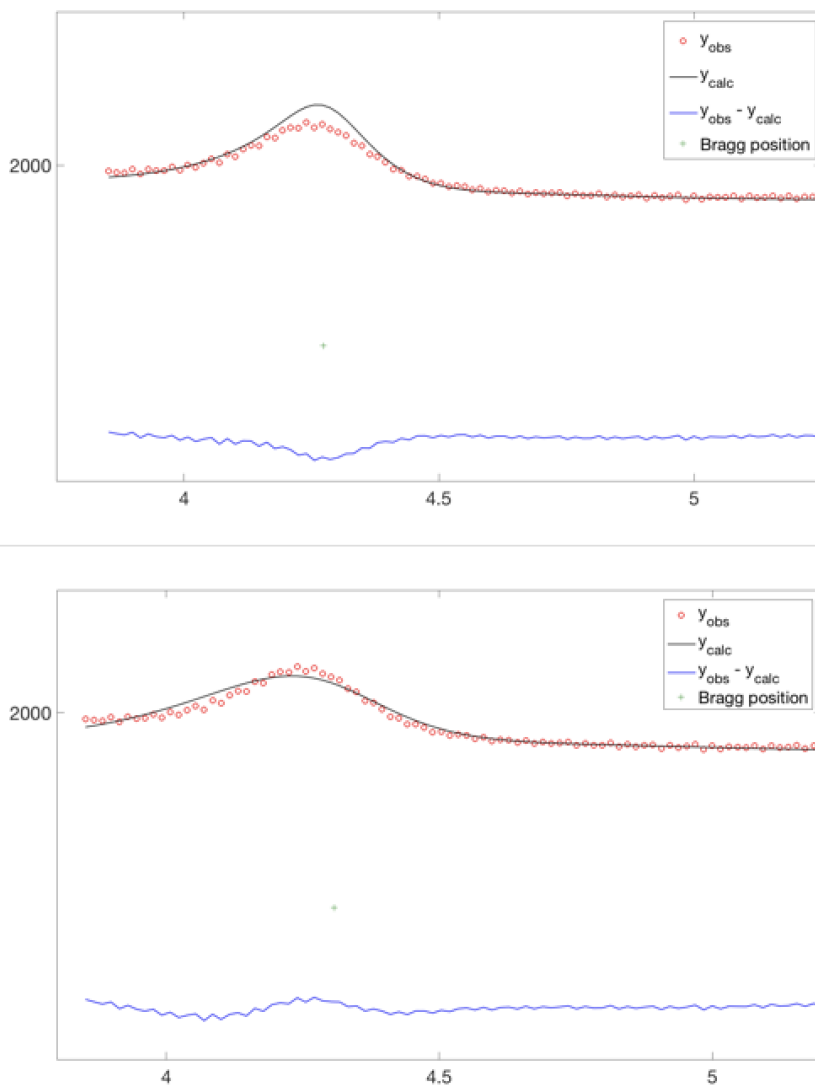
Figure 3.13: Rietveld fit of the (010) reflection without the asymmetric correction (top), and with the asymmetric correction (bottom). Improved fitting of the (010) reflection affected the amount of zinc in the interstitial 2b site by approximately 10%.
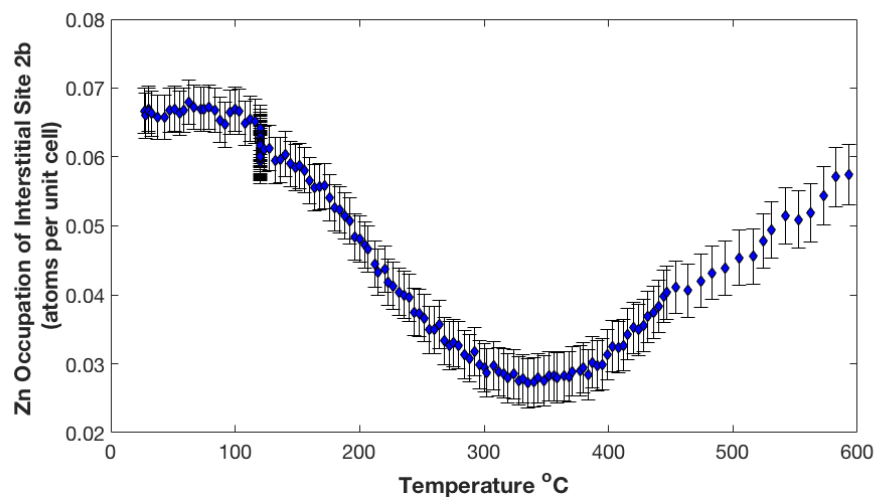
Figure 3.14: Zinc occupation of interstitial site 2b. The decrease of occupation around 100 °C correlates to an increase of zinc occupation in both site I and site II. The increase of occupation correlates to a slight decrease of zinc in site I and site II around 350 °C.

Volume Expansion

The volume behavior as a function of temperature is shown in Fig. 3.15. Compared to Fig. 3.1, the non-linearity in volume expansion during heating is more pronounced and can be attributed to the presence of zinc. A decrease in each of the "a" and "c" lattice parameters is observed at 120 °C, as shown in Fig. 3.16, due to surface water evaporation. Fig. 3.17 more clearly shows the deviation from linearity in volume and lattice parameters. These deviations were found by fitting a straight line to each of the volume, "a", and "c" parameters from 380 °C to 593 °C, where expansion was linear. The intercept corresponding to each of the slopes was calculated. Then, using $y = mx + b$ as a linear model, where x was the temperature data, values for volume, "a", and "c" parameters were calculated. The difference between those calculated values and the actual values were then plotted to show deviation from linearity for each parameter.

The decrease in lattice cell size is attributed to evaporation of surface water present in the sample. Compared to the unit cell volume and "a" parameter, this effect occurs to a much lesser extent in the "c" parameter. Compared to undoped HA, however, all changes in thermal expansion were more drastic. After heat treatment, the volume and lattice contractions were linear, matching those of undoped HA. This indicates that by the time the sample reaches maximum temperature, there is no more water present. Therefore during cooling, no water is absorbed. The nonlinear behavior, however, agrees with the presence of defect complexes consisting of cation vacancies, water, and zinc interstitials, Zn^{2b}-W^{VCaII} in ZnHA.[8]
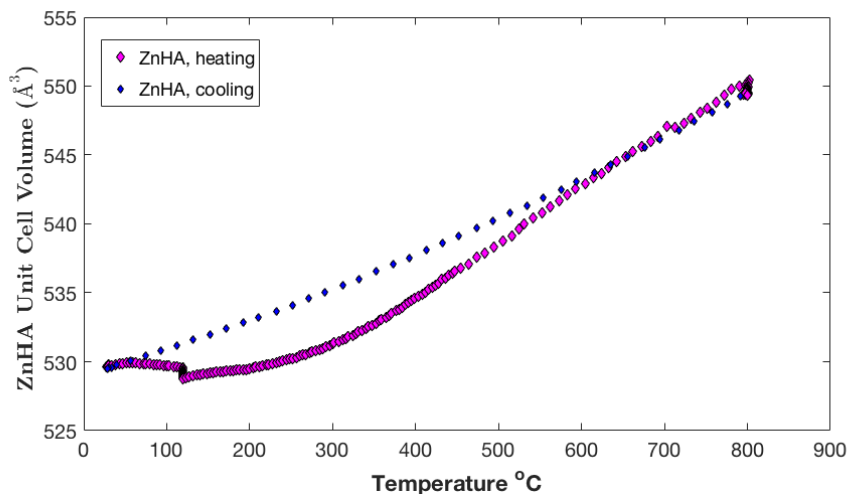
Figure 3.15: Unit cell volume of ZnHA through heating, and cooling of the sample. The nonlinearity in the volume is attributed to the presence of zinc in interstitial site 2b.
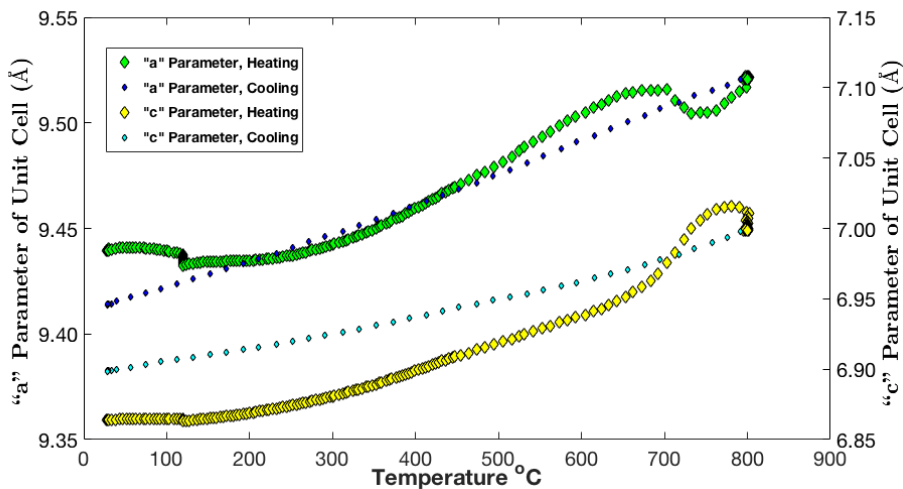

Figure 3.16: "a" and "c" parameters of ZnHA unit cell through heating, and cooling of the sample. There is a more significant change in the thermal evolution of the "a" parameter compared to the "c" parameter at 120 °C.
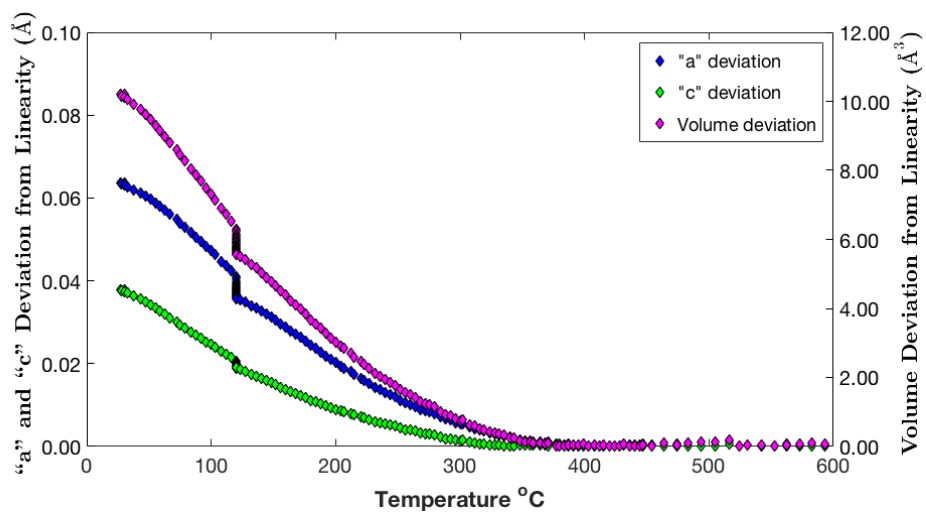
Figure 3.17: Deviation from linearity of the thermal evolution of ZnHA "a" parameter, "c" parameter, and volume. The changes in each are mostly linear from 350 °C until the end of the heating cycle.

Grain Size Behavior

The mean apparent size of ZnHA grains is shown in Fig. 3.18. The shape of zinc-doped HA grains, obtained from Rietveld refinement of 170 crystallographic reflections, was fairly anisotropic (as seen in Fig. 3.19), being 5-10 times larger in the (002) direction (as shown in Fig. 3.20) compared to the average grain size. Size anisotropy peaked at 350 °C, and then decreased at higher temperatures. The significant size and growth in the (002) crystal lattice direction, shown in Fig. 3.20, suggests a preferred orientation for ZnHA at high temperatures. This means that HA unit cells were aligned, or "stacked" preferentially along the (002) atomic planes, indicating a needle-like grain shape.

Compared to undoped HA, it seems that the zinc dopant inhibited the rapid growth in the (002) direction, seen in Fig. 3.5. Due to this effect, the corresponding anisotropy was limited, and was a factor of four times smaller than the anisotropy of the undoped HA sample (at peak values, comparing Figs. 3.4 and 3.19). The growth in the (002) direction, like undoped HA, dictates the behavior of the mean apparent grain size and the corresponding anisotropy. Compared to undoped HA, the growth in the (020) direction, as shown in Fig. 3.21, was also inhibited, and is actually slightly smaller after heat treatment. The mean apparent size of ZnHA grains, compared to undoped HA, is significantly smaller.
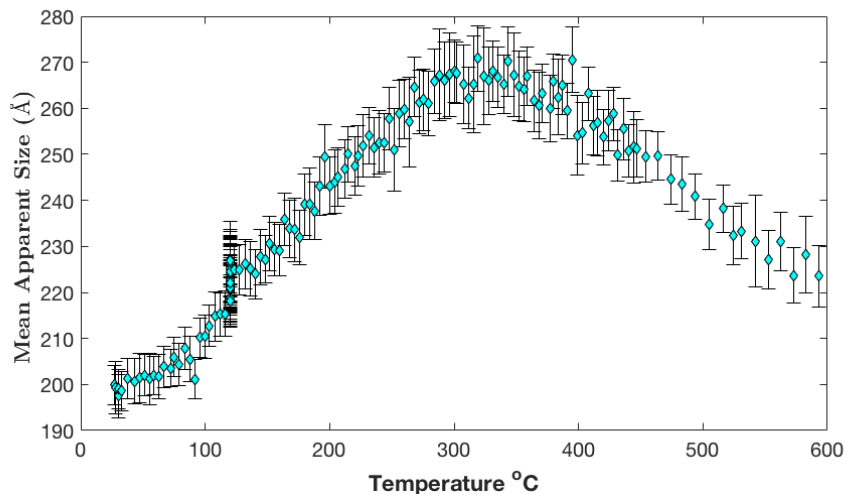
Figure 3.18: Mean apparent grain size during heating.
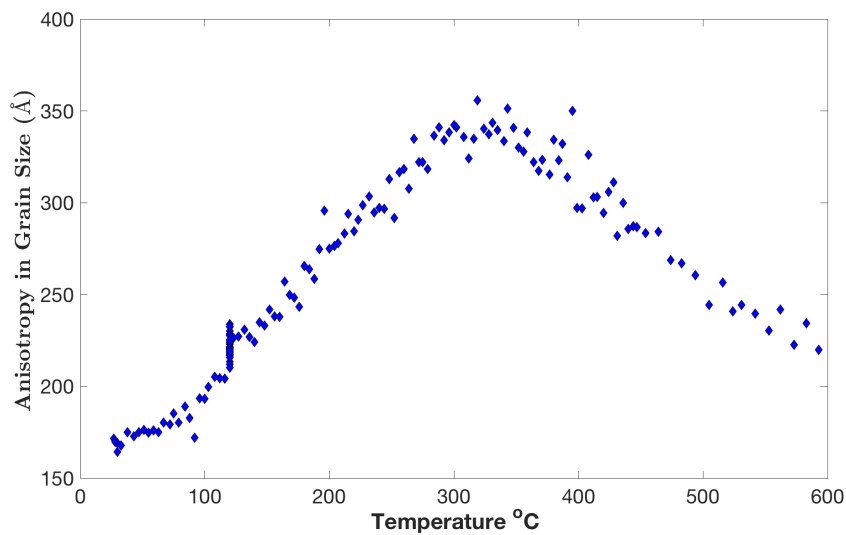

Figure 3.19: Anisotropy in the grain size of ZnHA. The anisotropy is the standard deviation of the apparent sizes obtained from the 170 measured reflections.
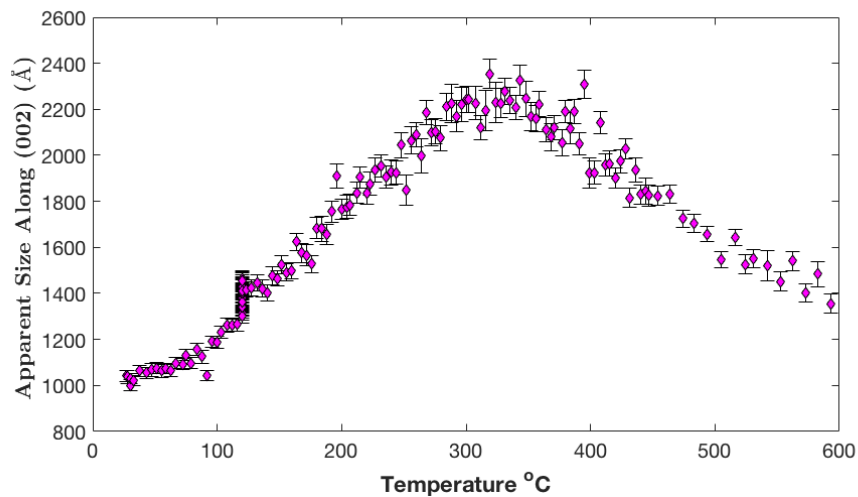
Figure 3.20: Thermal evolution in the direction of (002) planes in the ZnHA crystal lattice. The growth of the ZnHA grains in this direction peaks at approximately 300 °C.
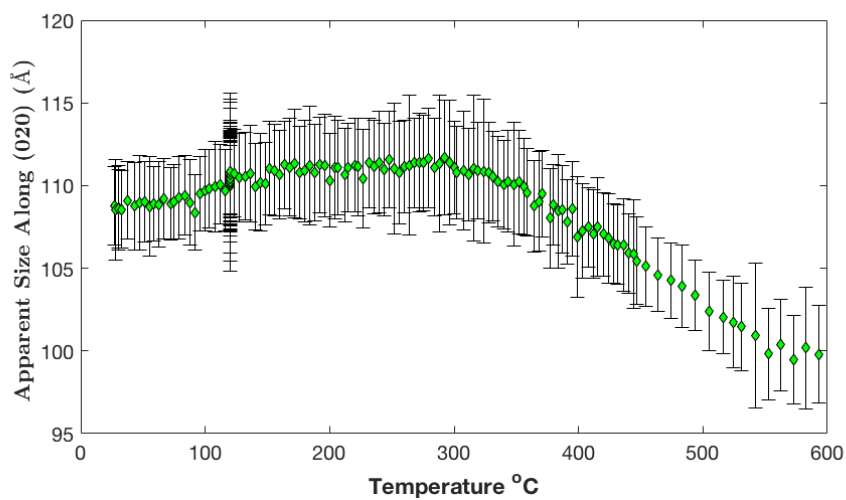

Figure 3.21: Thermal evolution in the direction of (020) atomic planes in the ZnHA crystal lattice. Throughout the heating cycle, there are only modest changes in the grain size along this direction.

3.4   Sr-doped HA, Model I

3.4.1   Refined Structural Parameters

For strontium-doped HA, the refined parameters included: unit cell "a" and "c" parameters, the atomic positions (shown in Table 1.1), the calcium and strontium occupancies, and the occupation of strontium at interstitial site 2b. As for the ZnHA sample, inclusion of an interstitial 2b site in the refinements resulted in an improved fit of the diffraction data, and a lower chi-squared in FullProf. As opposed to the ZnHA sample, however, there were no cation vacancies in the strontium-doped sample since models with cation vacancies always refined to a full occupation of sites I and II. The corresponding chemical equation is thus, $Ca_{10-x}Sr_x(PO_4)_6(OH)_2$ (where $x = 1$).

Two different refinements were done for this sample. The first scenario fixed the total occupation of site I + site II to 10, while letting the interstitial site refine freely. In the second scenario, site I and site II were fixed to their maximum occupancies of 4, and 6, while letting the interstitial site refine freely. In the first scenario, it was found that site II always refined to its maximum occupancy of 6. Site I was initially at its maximum occupancy of 4, but the occupation was not constant during the heating treatment. The following sections provide a discussion of the first scenario. An overview of the second scenario is given in the Appendix. As for ZnHA, other refinement models are currently being explored for the SrHA sample.

3.4.2   Thermal Evolution

Decomposition

Decomposition for both scenarios were the same, and SrHA was found to be significantly more stable than ZnHA. The sample decomposed into only α-TCP at a significantly higher temperature (790 °C), compared to ZnHA. In addition to higher stability, this sample retained the majority of its initial SrHA phase (approximately 90%) even after the formation of α-TCP, as shown in Fig. 3.22. This decomposition

is an interesting result for a variety of reasons. Decomposition into α-TCP at a relatively low temperature compared to other experiments, and without the presence of β-TCP, is highly uncommon.[5,12,13]
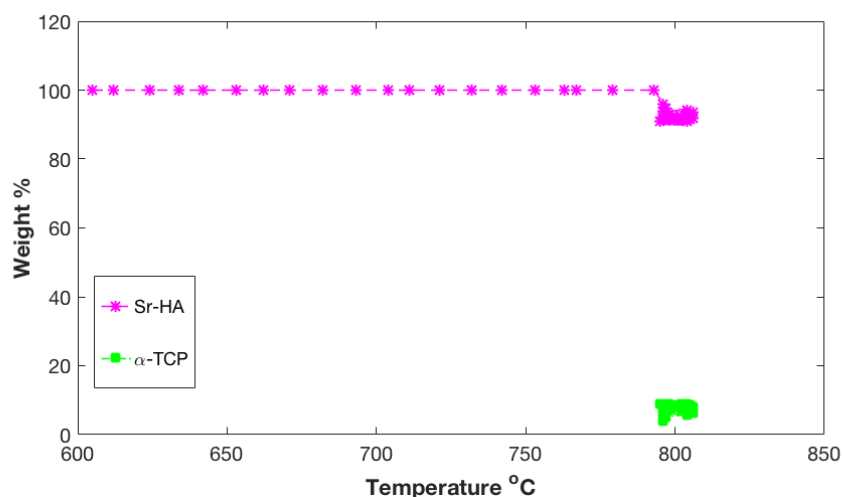

Figure 3.22: The fraction of SrHA and decomposition phases (HA and α-TCP) *vs.* heating temperature. SrHA has a late-onset decomposition, compared to ZnHA, occurring at approximately 790 °C.

Occupations of Cation Sites I and II

Consistent with the literature, the data show a clear preference for strontium substitution in the Ca II site, as shown in Fig. 3.23. Strontium occupation of site II peaks around 700 °C, and starts to decrease, while the occupation of site I is the smallest at 700 °C and then experiences a slight increase. The behavior of calcium in site I and site II are shown together in Fig. 3.24. The increase and subsequent decrease of strontium in site II correlates to a decrease, and subsequent increase of calcium in that site. Site I initially refined at maximum capacity (4), but lost a small amount of strontium and calcium in the formation of the α-TCP phase. As shown in Fig. 3.25, site II was always at maximum occupancy, while the occupation of site I decreased slightly during heating. After heat treatment and formation of the α-TCP phase, total occupancy for site I was mostly constant through the cooling

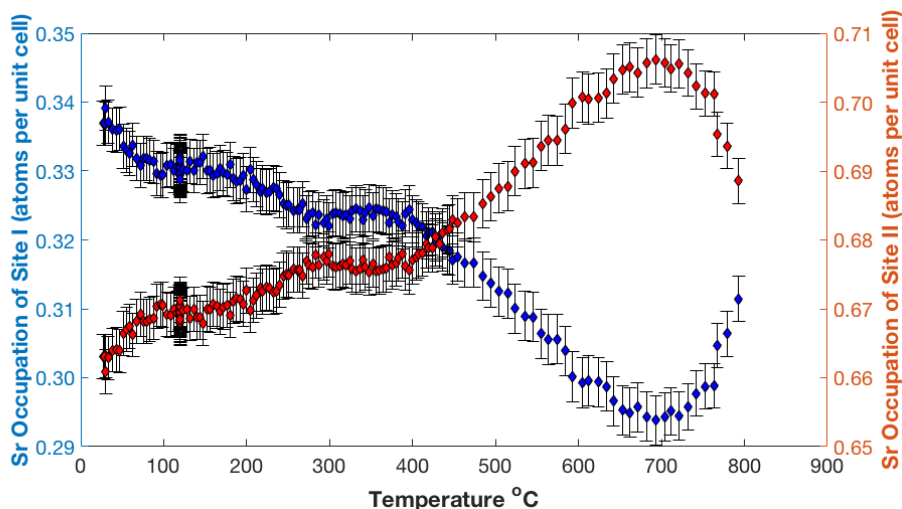cycle, while site II remained at maximum occupancy.

Figure 3.23: Strontium occupation of cation site I and site II. Site II is the preferred substitution site for strontium. The increase of strontium in site II from 400 °C to 700 °C is correlated to a decrease of calcium in site II.
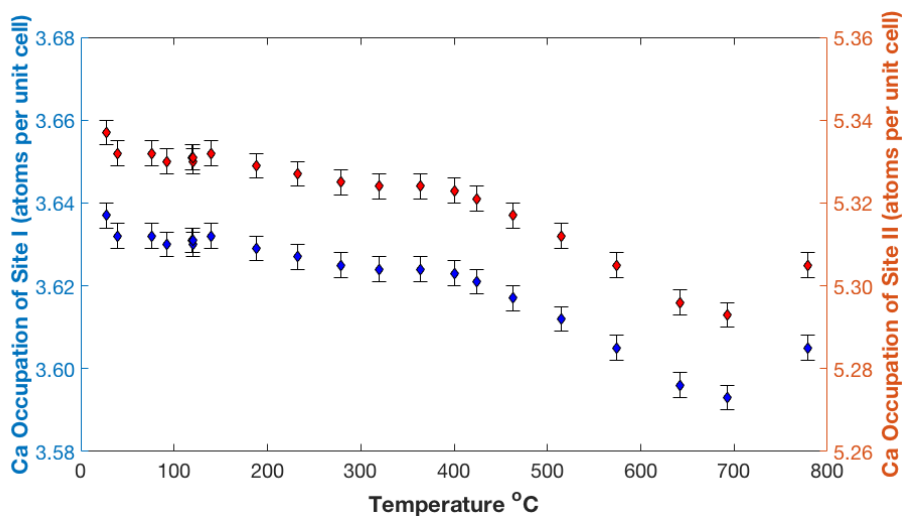

Figure 3.24: Calcium occupation of site I and site II within the HA unit cell. Calcium occupancies in each site remain fairly stable during cooling (not shown in this figure).
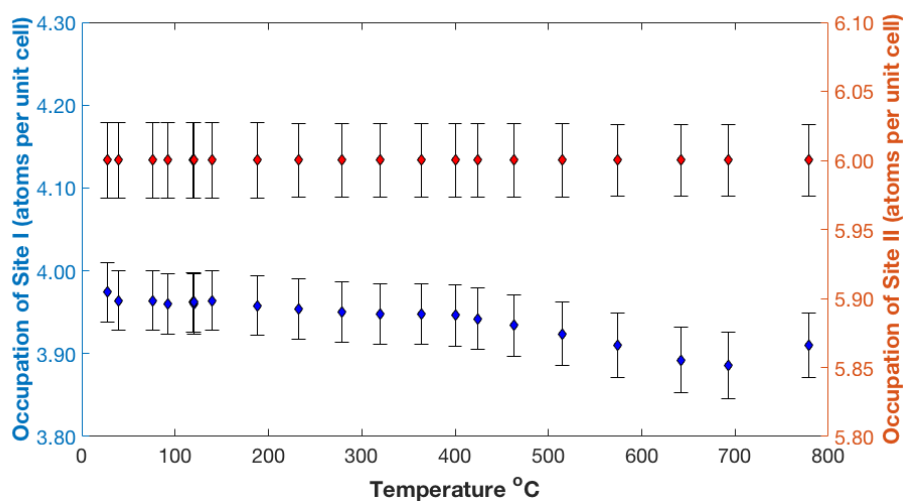
Figure 3.25: Total occupation (Sr + Ca) within the HA unit cell for site I and site II. Site II remains fully occupied throughout the temperature cycle.

Occupation of the 2b Interstitial Site

Similar to ZnHA, a special asymmetric correction to properly fit the (010) reflection had observable effects on the refined amount of strontium present in the interstitial site. However, 50% less strontium was present in the interstitial site (shown in Fig. 3.26), compared to the ZnHA sample. Furthermore, there was no strontium occupying the interstitial site by the end of heat treatment and onset of decomposition. All strontium incorporated into the HA lattice was either located in site I, site II, or was incorporated into the α-TCP phase by the time the sample had reached peak temperature. Based on the data, however, it seems likely that the loss of strontium in the interstitial site up to 400 °C corresponds to the increase of strontium in site II, while the decrease from 650 °C onward correlates to the slight increase of strontium in site I. Since so little strontium was present in the interstitial site, along with the absence of any cation vacancies, volume changes were mostly linear with the exception of surface water evaporation (around 100 °C), as shown in Fig. 3.27.
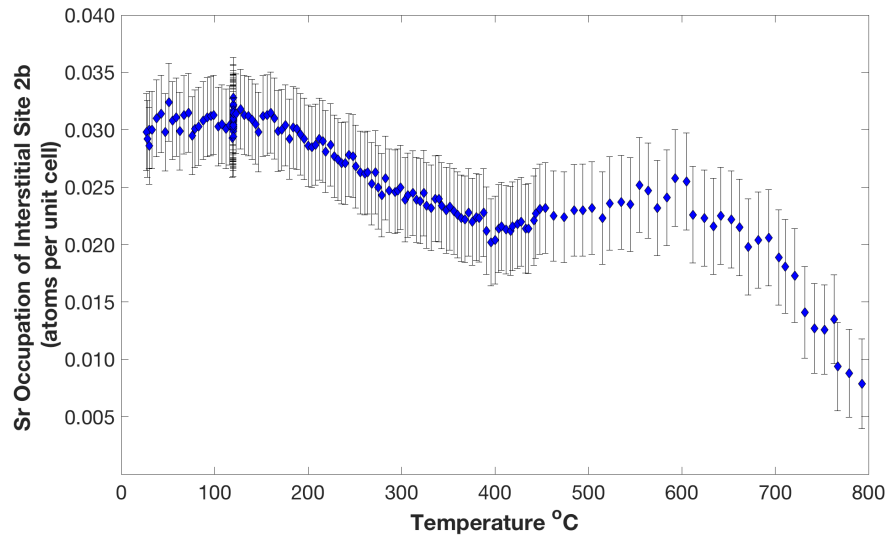

Figure 3.26: Strontium occupation of interstitial site 2b. Virtually no strontium was present in the interstitial site by the formation of the second phase (α-TCP) at 790 °C. The lower temperature decrease corresponds to an increase of strontium in site II, while the higher temperature decrease corresponds to an increase of strontium in site I.

Volume Expansion

There were no differences in the data for volume expansion in both refinements. The volume behavior of SrHA as a function of temperature is shown in Fig. 3.27. Similarly to undoped HA and ZnHA, there is a noticeable decrease in unit cell volume around 120 °C, attributed to the presumed evaporation of surface water in the sample. As seen in Fig. 3.28, unlike ZnHA, there is not a significant difference in the behavior of the "a", and the "c" parameters. The unit cell volume, "a", and "c" parameters all resemble the behavior of undoped HA (Fig. 3.2) rather than ZnHA. After heat treatment, the volume and lattice contractions were linear. This linearity indicates that the inclusion of strontium in the HA lattice is significantly more stable than the zinc substitution for calcium.
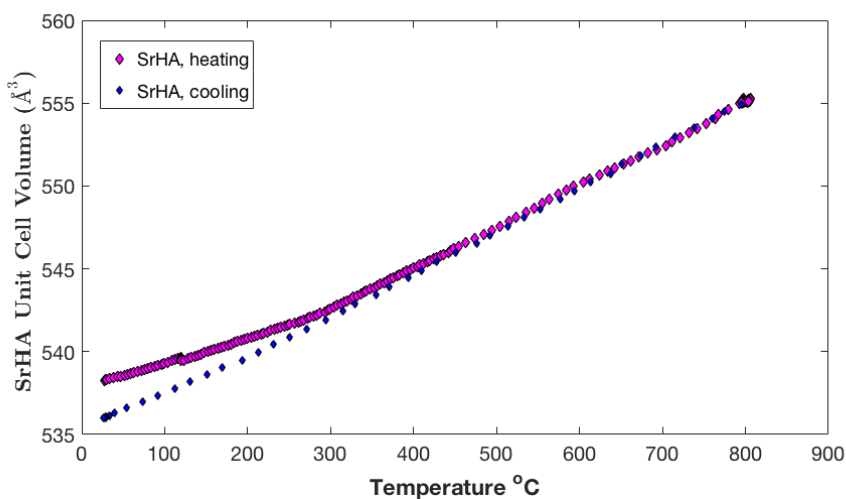

Figure 3.27: Unit cell volume of SrHA through heating and cooling of the sample. The trend in volume size resembles that of undoped HA. The presence of strontium does not seem to induce significant non-linear growth in the SrHA unit cell.
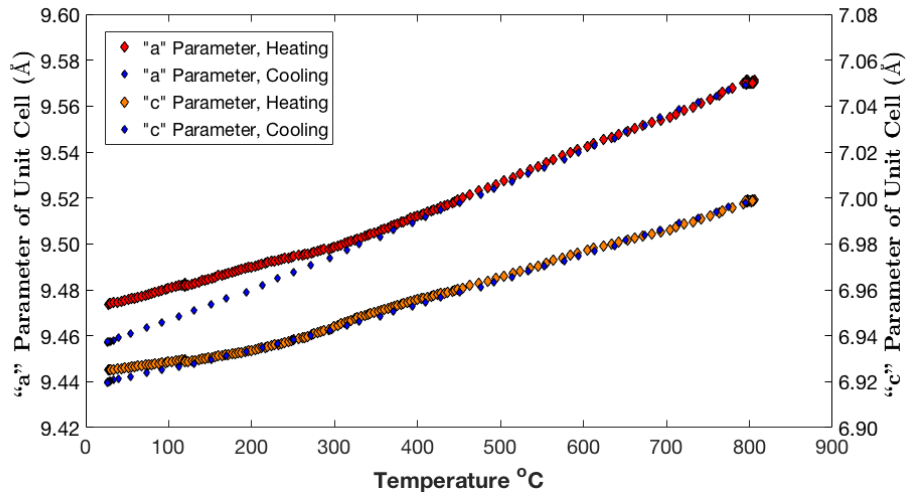
Figure 3.28: The "a" and "c" parameters of the SrHA unit cell through heating and cooling of the sample.

Grain Size Behavior

The mean apparent size of SrHA grains is shown in Fig. 3.29. Strontium-doped HA grains were found to be highly anisotropic (as shown in Fig. 3.30) compared to both undoped HA and ZnHA, and over 10 times larger along the (002) direction (as shown in Fig. 3.31) compared to the average grain size. Since even after decomposition, the majority of the sample was hydroxyapatite, data taken during sample cooling were included. There is a clear preferred orientation for SrHA at high temperatures, indicated by the significant growth along (002) shown in Fig. 3.31. Growth along (020) is shown in Fig. 3.32. Compared to both HA and ZnHA, the strontium dopant seemed to significantly induce an early rapid growth along (002). Even while the initial mean grain sizes were similar for both HA and SrHA, the anisotropy due to the rapid growth along the (002) planes was more pronounced in SrHA. The mean apparent grain size of SrHA was nearly three times as large as ZnHA, but still smaller than in undoped HA.
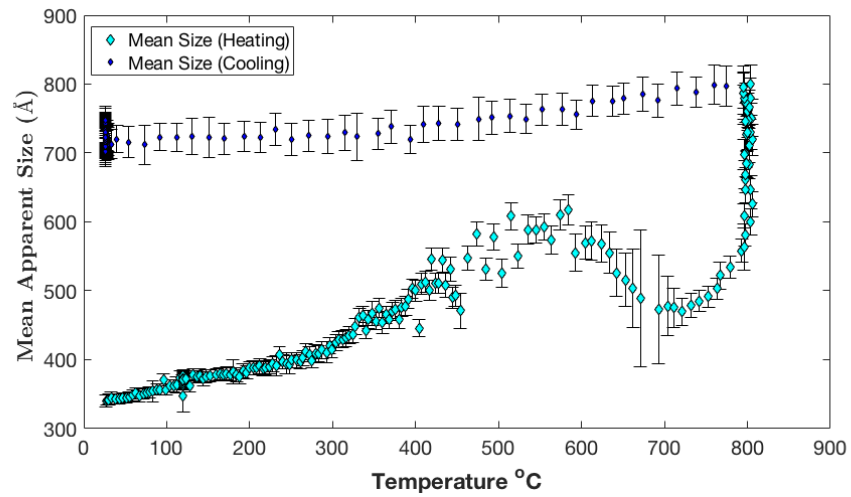
Figure 3.29: SrHA mean apparent grain size during heating and cooling.
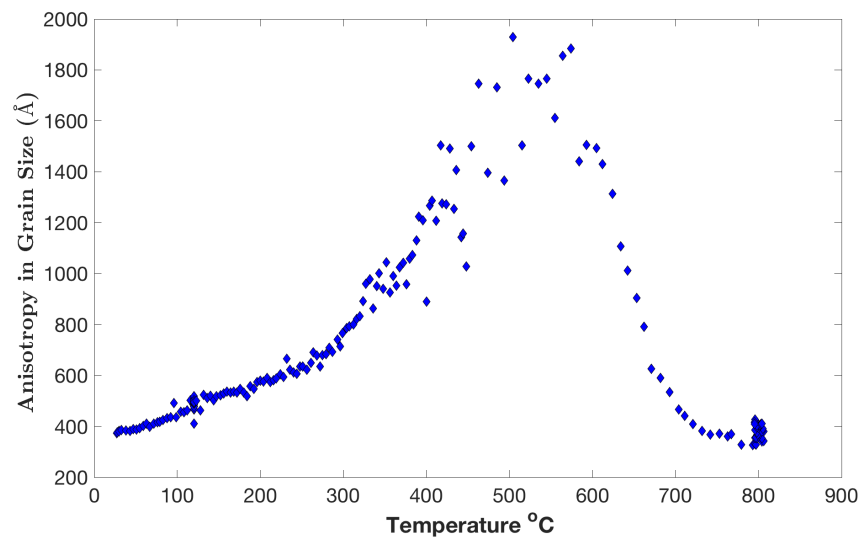
Figure 3.30: Anisotropy in the grain size of SrHA.

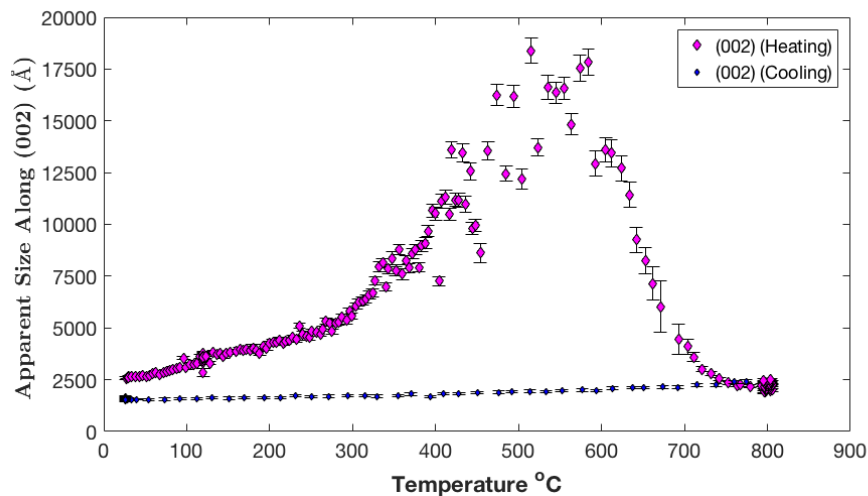Figure 3.31: Thermal evolution in the direction of (002) planes in the SrHA crystal lattice. The growth of the SrHA unit cell in this direction peaks at approximately 550 °C.
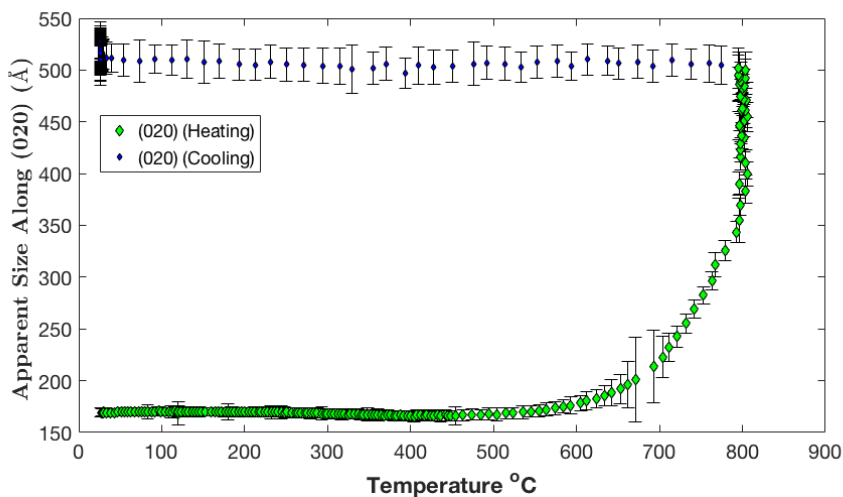

Figure 3.32: Thermal evolution in the direction of (020) atomic planes in the SrHA crystal lattice. The growth of the SrHA unit cell in this direction peaks at approximately 800 °C and remains stable throughout cooling.

3.5 Theoretical Modeling

Theoretical models for each of the HA samples were derived with Density Functional Theory (DFT) calculations for static structures by Dr. Terra and Dr. Ellis. Details of the calculations are found in reference 8. A brief summary of the results is presented here. All HA samples were initially hydrated, and throughout heat treatment they eventually became anhydrous due to water evaporation. Both hydrated, and anhydrous structural models were investigated. Formation energy calculations were performed for hydrated and anhydrous structures. Various Zn and water substitution scenarios in the presence of cation vacancies were considered, and the most energetically favorable structures were determined. The formation energy, E_{form}, is given by

$$E_{form} = E_{prod} - E_{rs} \tag{3.1}$$

where E_{rs} is the reference state. The product, E_{prod}, is dependent on Zn, water inclusion, and the defect type.

The calculations confirmed cation site II as the preferred substitution site for zinc, as well as the site most associated with entrained water. Of all hydrated and anhydrous ZnHA models, the model with substitutional ZnII and water at interstitial site $2b$ is the only one that accounts for the experimental behavior of the lattice parameters.[8] Theoretical models for SrHA are currently being explored.

CHAPTER 4

Conclusions

This project studied for the first time the *in-situ* thermal evolution of zinc-doped, strontium-doped, as well as undoped hydroxyapatite powder samples prepared via wet synthesis. Both dopants induced structural changes in HA, but Zn produced more drastic structural variations. Zinc occupied the Ca I, Ca II, and the 2b interstitial sites for ZnHA, but it preferred site II. Similarly, strontium was present in the cation and interstitial sites, but it preferred site II. The occupation of the interstitial site was smaller for Sr than Zn, and disappeared before decomposition. ZnHA was less stable than SrHA, and transformed at lower temperatures into TCP and ZnO phases. Decomposition of ZnHA started near 690 °C, and involved the formation of α-TCP, β-TCP, and ZnO. For SrHA, only α-TCP formed at 790 °C, and after decomposition the majority of the sample (90%) was still hydroxyapatite. A survey of *ex-situ* experiments found in the literature shows that there are conflicting results in the Zn doping mechanism. The discrepancy can be attributed to sample preparation and subsequent heat treatments. Undoped HA remained single-phase throughout the heating cycle. The volume expansions of undoped hydroxyapatite and SrHA were similar in that the expansions were considerably more linear than in ZnHA. After decomposition, lattice contractions for each sample were linear. These linear contractions indicate that during cooling, no additional water is incorporated into the structure. Furthermore, this attests to the comparatively higher stability of strontium in the HA lattice.

The behavior of ZnHA was in agreement with theoretical models in which the higher occupation of Zn interstitials and the presence of cation vacancies result in complex defect clusters that are linked to water dynamics and early onset of decomposition. This project validated the presence of these complex defect structures. Unit cell volume was the largest for SrHA, followed by ZnHA, and undoped HA. These find-

ings agree with the expected effects on the volume resulting from the substitution of a larger (Sr) and a smaller (Zn) atom into the HA lattice, respectively. Furthermore, compared to undoped HA, zinc seemed to inhibit average grain growth, while strontium seemed to have a smaller effect.

Two refinement scenarios for Sr were investigated. Both refinements have very similar chi-squared, and R_{bragg} values. Theoretical modeling for the SrHA data is still in progress, and should play a vital role in determining the better refinement. Based on both refinements, however, it is clear the strontium occupation of the interstitial site is only 50% of the zinc occupancy, and that within experimental error, no vacancies exist. Furthermore, the nearly linear lattice expansions and contractions in SrHA correlate well with the absence of the defect complexes that are present in ZnHA. Some biomedical applications prefer HA which is more biocompatible, while others prefer tricalcium phosphate which is more bioresorbable, *in-vivo*. It is then sometimes preferable to produce a biphasic material (HA + TCP) which can be obtained by high-temperature annealing of Zn- and Sr-doped HA. In clinical applications, Zn and Sr doping amounts would likely be less than 2 at. %, because any higher concentrations could be toxic. Higher doping amounts reveal which phases form more quickly as a function of annealing temperature and provide important information about sample stability in general. Therefore, these results provide valuable insight on the stability of zinc and strontium dopants. This research was solely focused on samples with 10 at. % doping concentrations, and numerous samples with varying doping levels, and dopants were also prepared. Given the novelty of *in-situ* studies, and the detailed information provided from them, it will be exciting to monitor the progress of ongoing HA research on different samples.

Appendix

Sr-doped HA, Model II

Refined Structural Parameters

In the second strontium refinement, site I and site II were fixed at their maximum occupancies of 4, and 6, while the interstitial site was freely refined. The following provides a comparison between the two refinements with a primary focus on the data that show significant differences in results.

Thermal Evolution

Occupations of Cation Sites I and II

In this scenario, fixing each site to maximum occupancy showed a large deviation in the behavior of strontium occupancy of site II, as seen in Fig. A.1. While the preference for site II is consistent with the literature, there are no reports of such high strontium occupancies for site II. This data implies that the SrHA sample was "saturated" to an extent, meaning that it contained more than 10 at. % strontium initially. The behavior of calcium in site I and site II is shown in Fig. A.2. The significant increase of strontium in site II signals a decrease of calcium in site II, the value of which is much lower than in the first refinement.
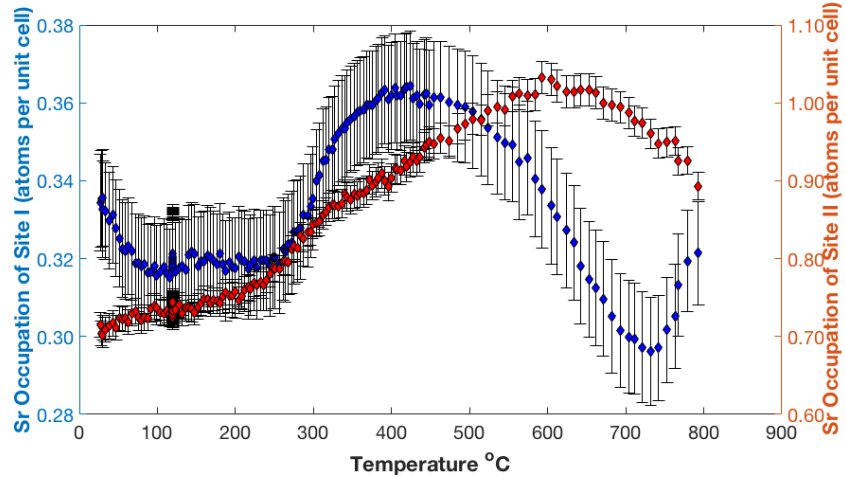
Figure A.1: Strontium occupation of cation site I and site II. Site II is the preferred substitution site for strontium. Between 550°C and 700°C, approximately 10at% of strontium is in site II. During the majority of the heating process, the total strontium in the sample is greater than 10 at. %.
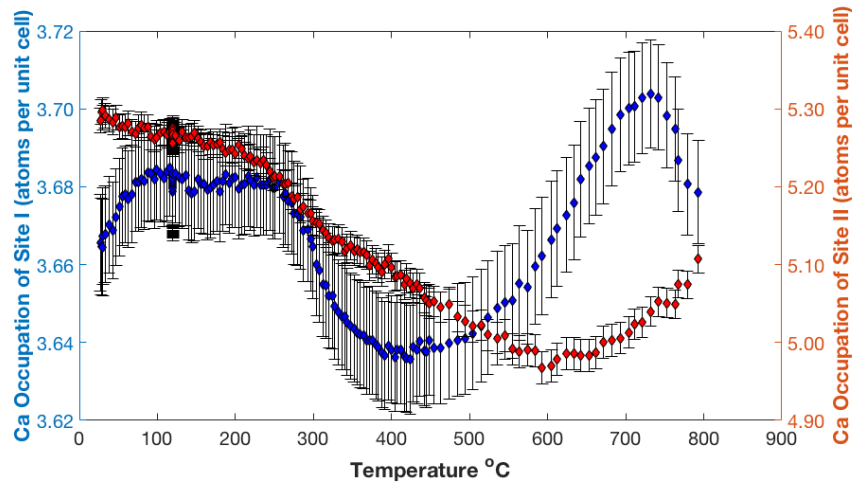

Figure A.2: Calcium occupations of site I and site II within the HA unit cell. Corresponding the increase of strontium in site II is the significant decrease of calcium in site II.

Occupation of the 2b Interstitial Site

The behavior of strontium in interstitial site 2b for the second refinement is seen in Fig. A.3. In both refinements, there was no strontium in the interstitial site by the end of heat treatment. However, in this scenario, the amount of strontium in the site was noticeably more stable up until 600 °C, after which a more drastic exhaustion of interstitial strontium took place as compared to the first scenario.
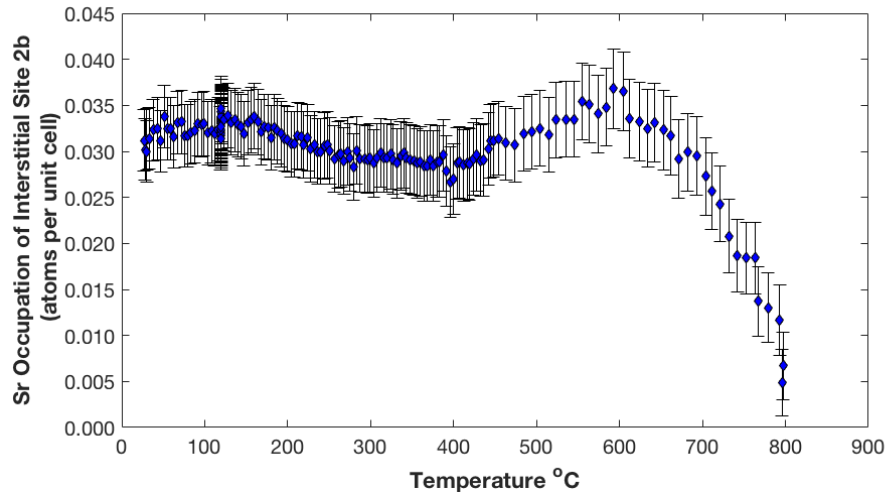

Figure A.3: Strontium occupation of interstitial site 2b. As in refinement I, no strontium was present in the interstitial site by the formation of the second phase (α-TCP) at 790 °C.

Bragg Factor Comparisons

Figs. A.4 and A.5 show the R_{Bragg} values for each scenario through heat treatment. The second refinement is slightly better, as the majority of R_{Bragg} values refine lower for longer throughout heating compared to those in the first refinement.
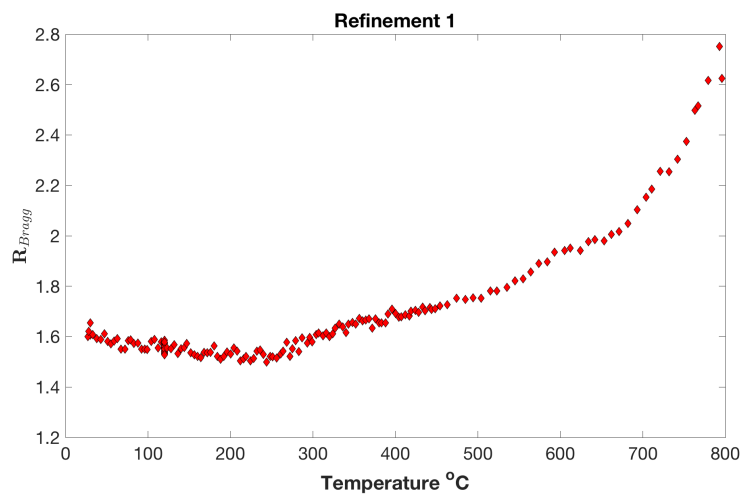

Figure A.4: R_{Bragg} values for the first SrHA scenario, where the total amount of strontium and calcium in sites I and II was fixed to 10.
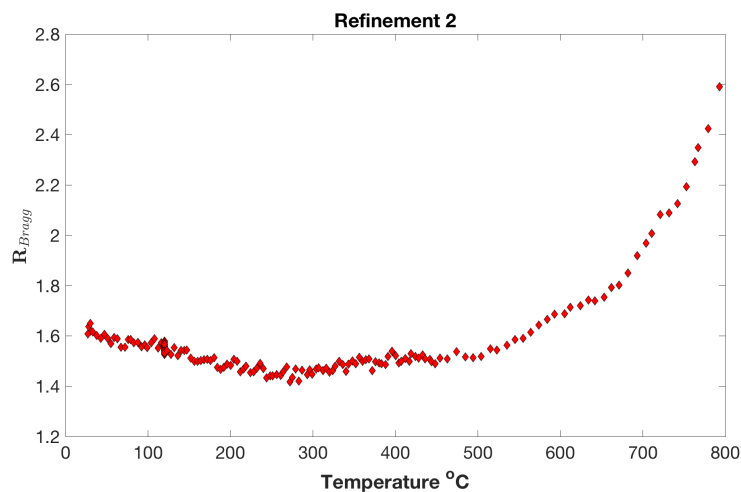

Figure A.5: R_{Bragg} values for the second SrHA scenario, where site I and site II were fixed to their maximum occupancies of 4 and 6.

References

[1] Shepherd, J.H., Shepherd, D.V., and Best, S. (2012). Substituted hydroxyapatites for bone repair. *J Mater Sci: Mater Med*, **23**, 2335-2347.

[2] Kay, M.I., Young, R.A., and Posner, A.S. (1964). Crystal structure of hydroxyapatite. *Nature* **204**, 1050-1052.

[3] Gomes, S., Nedelec, J., Jallot, E., Sheptyakov, D., and Guillaume, R. (2011). Unexpected Mechanism of Zn^{2+} insertion in calcium phosphate bioceramics. *Chem. Mater.*, **23**, 3072-3085.

[4] Matsunaga, K., Murata, H. Mizoguchi, T., and Nakahira, A. (2009). Mechanism of incorporation of zinc into hydroxyapatite. *Acta Biomaterialla*, **6**, 2289-2293.

[5] Terra, J., Dourado, E.R., Eon, J.G., Ellis, D.E., Gonzalez, G., and Rossi, A.M. (2009). The structure of strontium-doped hydroxyapatite: an experimental and theoretical study. *Phys Chem Chem Phys*, **11**(3), 568-577.

[6] Landi, E., Logroscino, G., Proietti, L., Tampieri, A., Sandri, M., and Sprio, S. (2008). Biomimetic Mg-substituted hydroxyapatite: from synthesis to in vivo behaviour. *J Mater Sci Mater Med*, **19**(1), 239-247.

[7] Sun, Z., Wataha, J., and Hanks, C. (1997). Effects of metal ions on osteoblast-like cell metabolism and differentiation. *J Biomed. Mater. Res.*, **34**, 29-37.

[8] Gonzalez, G., Terra, J., Smith, D., Kiverkis, U., Di Maso, L., Wilson, N., Okasinski, J., Rossi, A.L., Ellis, D., and Rossi, A.M. (*In Preparation*). The structure of Zn doped hydroxyapatite revisited: thermal evolution from hydrated phase to decomposition using in-situ x-ray diffraction. Experiment and theory.

[9] Miyaji, F., Kono, Y., and Suyama, Y. (2004). Formation and structure of zinc-substituted calcium hydroxyapatite. *Mater. Res. Bull.*, **40**, 209-220.

[10] Bigi, A., Foresti, E., Gandolfi, M., Gazzano, M., and Roveri, N. (1995). Inhibiting effect of zinc on hydroxylapatite crystallization. *J. Inorg. Biochem.*, **58**, 49-58.

[11] Mayer, I. and Featherstone, J.D.B. (2000). Dissolution studies of Zn-containing carbonated hydroxyapatites. *J. Cryst. Gr.*, **219**, 98-101.

[12] Bigi, A., Boanini, E., Capuccini, C., and Gazzano, M. (2006). Strontium-substituted hydroxyapatite nanocrystals. *Inorg. Chim. Acta*, **360**, 1009-1016.

[13] Kumar, P., Mishra, S., Kiran, R., and Kannan, S. (2015). Preferential occupancy of strontium in the hydroxyapatite lattice in biphasic mixtures formed from non-stoichiometric calcium apatites. *Dalton Trans.*, **44**, 8284-8292.

[14] Kottegoda, N., Munaweera, I., Madusanka, N., and Karunaratne, V. (2011). A green slow-release fertilizer compositon based on urea-modified hydroxyapatite nanoparticles encapsulated wood. *Current Science* vol. **101**, no.1, 73-78.

[15] Sneddon, I.R., Orueetxebarria, M., Hodson, M.E., Schofield, P.F., and Valsami-Jones, E. (2006). Use of bone meal amendments to immobilise Pb, Zn, and Cd in soil: A leaching column study. *Environmental Pollution*, **144**, 816-825.

[16] Chupas, P., Chapman, K., Kurtz, C., Hanson, J., Lee, P., and Grey, C. (2008). A versatile sample-environment cell for non-ambient X-ray scattering experiments. *J. App. Cryst.*, **41**, 822-824.

[17] Toby, B. and Von Dreele, R. (2013). GSAS-II: The genesis of a modern open-source all purpose crystallography software package. *J. App. Cryst.*, **46**, 544-549.

[18] Rietveld, H.M. (1967). Line profiles of neutron powder-diffraction peaks for structure refinement. *Acta Cryst.*, **22**, 151.

[19] Rietveld, H.M. (1969). A profile refinement method for nuclear and magnetic structures. *J. App. Cryst.*, **2**, 65-71.

[20]   Rodríguez-Carvajal,   J.   (2001).   FullProf   Suite,
http://www.ill.eu/sites/fullprof/index.html.

[21] Rodríguez-Carvajal, J. (2001). Recent developments of the program FullProf.
Commission on Powder Diffraction, IUCr, Newsletter **26**.

Acknowledgments